Multiwavelength observations of cirrus clouds in the North Celestial Loop: the transition from atomic to molecular gas

L. Barriault, Gilles Joncas, Edith Falgarone, D. J. Marshall, M. Heyer, Francois Boulanger, Tyler Foster, C. Brunt, Marc-Antoine Miville-Deschenes, K. Blagrave, et al.

Monthly Notices
of the
ROYAL ASTRONOMICAL SOCIETY

Mon. Not. R. Astron. Soc. **406,** 2713–2731 (2010) doi:10.1111/j.1365-2966.2010.16871.x

Multiwavelength observations of cirrus clouds in the North Celestial Loop: the transition from atomic to molecular gas

L. Barriault,[1⋆] G. Joncas,[1⋆] E. Falgarone,[2⋆] D. J. Marshall,[1⋆] M. Heyer,[3⋆] F. Boulanger,[4⋆] T. Foster,[5⋆] C. Brunt,[6⋆] M.-A. Miville-Deschênes,[4] K. Blagrave,[7] R. Kothes,[8] T. L. Landecker,[8] P. G. Martin,[7] D. Scott,[9] J. M. Stil[10] and A. R. Taylor[10]

[1]*Département de physique, de génie physique et d'optique and Centre de recherche en astrophysique du Québec (CRAQ), Université Laval, Québec, QC G1V 0A6, Canada*
[2]*École Normale Supérieure and Observatoire de Paris, 24 rue Lhomond, 75231 Paris, Cedex 05, France*
[3]*Department of Astronomy, University of Massachusetts, Amherst, MA 01003-9305, USA*
[4]*Institut d'Astrophysique Spatiale, Université Paris-Sud, 91405 Orsay, France*
[5]*Department of Physics and Astronomy, Brandon University, Brandon, MB R7A 6A9, Canada*
[6]*School of Physics, University of Exeter, Stocker Road, Exeter EX4 4QL*
[7]*Canadian Institute for Theoretical Astrophysics, University of Toronto, ON M5S 3H8, Canada*
[8]*National Research Council of Canada, Herzberg Institute of Astrophysics, Dominion Radio Astrophysical Observatory, PO Box 248, Penticton, BC V2A 6J9, Canada*
[9]*Department of Physics and Astronomy, University of British Columbia, Vancouver, BC V6T 1Z1, Canada*
[10]*Department of Physics and Astronomy, University of Calgary, 2500 University Drive NW, Calgary, AB T2N 1N4, Canada*

Accepted 2010 April 19. Received 2010 April 15; in original form 2010 February 17

ABSTRACT

Two potential sites of H_2 formation have been discovered in diffuse gas at high Galactic latitude through examining the far-infrared (FIR) H I ratio and looking for an excess over that expected from an atomic medium. We call these the Spider and Ursa Major fields. New ^{12}CO and ^{13}CO Five College Radio Astronomical Observatory observations are presented for both regions (53 936 spectra in the Spider and 23 517 spectra in Ursa Major). Although there is a correlation between FIR excess and CO emission, we find that the FIR excess peaks do not coincide with the ^{12}CO emission peaks, indicating that CO might be a poor tracer of H_2 in diffuse regions. This implies (i) that the density is too small to allow CO excitation, (ii) that the CO self-shielding is insufficient or (iii) local variations of the dust properties. The ^{12}CO observations are compared with H I observations from the Dominion Radio Astrophysical Observatory. We decompose the 10 000 H I profiles of the Spider and the 20 302 H I profiles of Ursa Major into Gaussian components. We always find at most two narrow components and one broad component. CO always seems to appear where two H I velocity components merge or where there is a H I velocity-shear.

Key words: ISM: clouds – ISM: molecules – infrared: ISM – radio lines: ISM.

1 INTRODUCTION

The observation of the sky by *IRAS* has allowed the discovery of extended far-infrared (FIR) sources superposed on the IR background at high Galactic latitudes (Low et al. 1984). Those sources are called IR cirrus clouds and are associated with diffuse H I clouds seen in the high Galactic latitude H I surveys (Heiles & Habing 1974; Heiles 1975; Stark et al. 1994; Hartmann & Burton 1997). Some of those IR cirrus clouds are also linked to molecular clouds (Blitz, Magnani & Mundy 1984; Magnani, Hartmann & Speck 1996). A number of early studies have been carried out to better understand the complex structure seen in the *IRAS* images. Whereas a correlation between the 100 μm FIR intensity and the H I column density was observed in some atomic cirrus clouds (Boulanger, Baud & van Albada 1985; Boulanger & Perault 1988; Boulanger et al. 1996), Weiland et al. (1986) also demonstrated the existence of a correlation between the 100 μm IR emission and the CO integrated intensity in molecular cirrus clouds. Driven by the fact that the dispersion around the FIR–H I correlation is larger than the uncertainties (Désert, Bazell & Boulanger 1988), it was later shown that the FIR intensity is

⋆E-mail: leo.barriault.1@ulaval.ca (LB); joncas@phy.ulaval.ca (GJ); edith@lra.ens.fr (EF); douglas.marshall.1@ulaval.ca (DJM); heyer@astro.umass.edu (MH); francois.boulanger@ias.u-psud.fr (FB); fostert@Brandonu.ca (TF); brunt@astro.ex.ac.uk (CB)

strongly correlated with the total gas density (H I and H_2). The presence of H_2 in these cirrus clouds was subsequently inferred indirectly by looking at an IR excess over the IR intensity expected from a purely atomic medium (Joncas, Boulanger & Dewdney 1992; Reach, Koo & Heiles 1994; Reach, Wall & Odegard 1998). H_2 has been observed directly only for a few locations by looking at the H_2 absorption towards high-latitude AGN (Gillmon & Shull 2006).

Among the high Galactic latitude clouds catalogued by Dutra & Bica (2002), 90 per cent are 'diffuse' ($A_V < 1$) (McGehee 2008), whereas 10 per cent are 'translucent' ($A_V = 1$–5) (Magnani et al. 1996) and only one is a dark cloud (MBM12, $A_V > 5$). As strong turbulence opposes self-gravity in the cirrus clouds, it was first supposed that such clouds are unable to form stars (Heithausen 1996). However, more recently, gravitationally bound cores have been found in a cirrus cloud located in the Polaris Flare (Heithausen, Bertoldi & Bensch 2002), and star formation has been confirmed in two high Galactic latitude clouds, MBM 12 and MBM 20 (McGehee 2008, and references therein). Nevertheless, most cirrus clouds appear to be devoid of stars which makes them useful sites for studying the physical processes that influence the interstellar medium before star formation turns on. Miville-Deschênes et al. (2002) showed that the dynamics of those cirrus clouds affect dust evolution and therefore molecule formation, since dust is a catalyst in molecule formation. Therefore, the cirrus clouds with high molecular abundance are probably in a transition state between atomic and molecular phases and are the best cloud targets for studying this transition.

The H I–H_2 transition in cirrus clouds has been characterized by numerous *Far Ultraviolet Spectroscopic Explorer* (*FUSE*) observations towards extragalactic UV sources, which provide direct measurements of the H_2 column density (Gillmon et al. 2006; Wakker 2006). The fraction of H_2 gas is observed to be significant for hydrogen column densities larger than 2–3 $\times$ 10^{20} cm^{-2}. The *FUSE* data has been interpreted within models where the H_2 fraction is set by the local equilibirum between H_2 formation on dust grains and photo-dissociation by UV light. Within these models, the H_2 fraction and the ratio between the $J = 0$ and 1 H_2 column densities are both accounted for with gas densities smaller than 100 H cm^{-3} (Gry et al. 2002; Gillmon & Shull 2006; Nehmé et al. 2008). However, since the H_2 formation and photo-dissociation time-scales ($>10^7$ yr) are larger than the dynamical time-scales associated with interstellar turbulence on the scales of the absorbing clouds (Gry et al. 2002), the H I–H_2 transition may be primarily driven by cloud dynamics.

Some multidimensional simulations were done to understand the formation of molecular clouds (e.g. see the review by Hennebelle, Mac Low & Vazquez-Semadeni 2009). One idea is that molecular clouds are formed where two warm atomic hydrogen gas flows collide. Hennebelle et al. (2008) present the results of magnetohydrodynamic simulations of such colliding flows. Those flows trigger thermal instability that could lead to gravitational collapse. A transition between warm atomic hydrogen gas and dense gas occurs due to thermal instability and cooling. Glover & Mac Low (2007) performed hydrodynamical simulations with a supersonically turbulent initial velocity field and show that large amounts of H_2 are formed from atomic gas on time-scales of 1–2 Myr in turbulent gas.

Many complex molecules have been found in diffuse clouds through millimetre spectroscopy (Liszt, Lucas & Pety 2005, and references therein). Models for homogeneous media (van Dishoeck & Black 1986) and for inhomogeneous media (Spaans 1996) have been used to reproduce the observed physical conditions. Whereas the abundance distributions of OH, CN, C_2 and CH are well explained by models of diffuse cloud chemistry, it is difficult to reproduce other molecule abundances, like those of CH^+ or HCO^+, because energy sources larger than the average thermal energy found within diffuse clouds are needed (Cecchi-Pestellini, Casu & Dalgarno 2005). However, hot chemistry is possible in models involving intermittency in a turbulent gas (Falgarone & Puget 1995; Falgarone, Pineau des Forets & Roueff 1995) as well as in models involving shocks (Flower & Pineau des Forets 1998).

Physical conditions in cirrus clouds are not well understood. van Dishoeck et al. (1991) conclude that translucent clouds have low gas volume densities ($n = n(H) + n(H_2) = 200$–$5000\,\mathrm{cm}^{-3}$) and high kinetic temperatures ($T_k > 20$ K) and this was confirmed by Turner, Terzieva & Herbst (1999, and references therein). On the other hand, Falgarone & Phillips (1996) found high densities ($n > 10^4\,\mathrm{cm}^{-3}$) and small kinetic temperatures ($T_k < 15$ K) towards the Perseus-Auriga cloud edges.

To better understand the environment associated with zones of molecule formation, H I line, ^{12}CO ($J = 1 - 0$) and ^{13}CO ($J = 1 - 0$) observations are presented for diffuse gas located in a prominent H I loop towards the north celestial pole called the North Celestial Loop (NCL) (Meyerdierks, Heithausen & Reif 1991). Two cirrus clouds shown in Fig. 1 were observed: a diffuse cloud located at the centre of the field (large polygon), which we refer to as the Spider after its morphology, and the eastern part of the Ursa Major cirrus structure located at larger Galactic longitudes than the first field (small polygon). The distance of those cirrus clouds is $\approx$100 pc, uncertain by a factor of 2 (de Vries, Thaddeus & Heithausen 1987). Whereas there are no previous investigations of the Spider, a few studies have been carried out on the Ursa Major clouds (de Vries et al. 1987; Joncas et al. 1992; Pound & Goodman 1997; Miville-Deschênes et al. 2003).

In this paper, we will first examine the correlation between the H I and the *IRAS* IR emission to find potential sites of H_2 formation in both regions. We will then present new complementary ^{12}CO and ^{13}CO observations (integrated intensity and velocity fields) from the Five College Radio Astronomical Observatory (FCRAO) at those two locations. These data will be used to determine the H_2 column density and mass and the comparison with H I observations from the Dominion Radio Astrophysical Observatory (DRAO) will

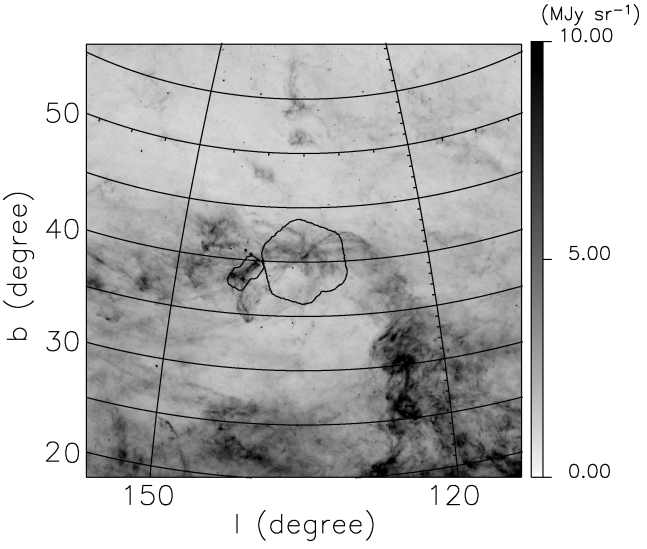

Figure 1. Global view of the NCL in *IRAS* 100 μm emission. The H I Spider field is located in the large polygon. The H I Ursa Major field is located in the small polygon.

Table 1. Parameters of the H I DRAO data cubes.

	Spider	Ursa Major
Channel separation (km s^{-1})	0.824	0.412
Number of channels	256	64
Angular resolution (arcmin)	1.0×1.06	1.0×1.06
Arcmin pixel^{-1}	0.3	0.5
rms noise (K)	1	3
Observation date	2007	1989 and 1994

allow a better understanding of transition zones between atomic and molecular hydrogen and CO. The Spider H I data come from the DRAO Planck Deep Fields (DPDF) observations. This project was initiated in order to better understand the contribution of the Milky Way ISM to Planck foreground contamination and high Galactic latitude gas physics. This project will be fully described in Martin et al. (in preparation).

This paper is the first of a series of three papers that will look at the transition between atomic and molecular gas in diffuse cirrus clouds. It is structured as follows. In Section 2, the observations and the data processing techniques are outlined. In Section 3, the results are described for each object in turn. Finally, in Section 4, the results are discussed. We conclude in Section 5.

2 OBSERVATIONS AND DATA PROCESSING

The DRAO interferometer is an array of seven 9-m paraboloids on a 600-m east–west baseline (Landecker et al. 2000). As three antennas can move, 140 baselines from 12.9 to 617.1 m are available. The field of view is 2.°6 while the synthesized beam is 0.98×1.02 arcmin^2. The low spatial frequency H I data were obtained with the 26-m DRAO single dish telescope. The final data are a combination of the synthesis data and the 26-m single dish data allowing complete coverage of the u–v plane (Taylor et al. 2003). The characteristics of the data products are listed in Table 1. The data are gridded to produce maps having 18 arcsec pixel^{-1} for the Spider and 30 arcsec pixel^{-1} for Ursa Major. While the channel spacing is 0.824 and 0.412 km s^{-1} for the Spider and Ursa Major, respectively, the spectral resolution is 1.32 and 0.66 km s^{-1} for each field. The Ursa Major data were obtained in 1989 and 1994 (Joncas et al. 1992; Miville-Deschênes et al. 2003) using the DRAO. To increase the signal-to-noise ratio (S/N), they have been filtered prior to this analysis (Miville-Deschênes et al. 2003), using a method based on a wavelet decomposition of each channel (Starck & Murtagh 1998). The new Spider data were obtained in 2007 by observing 58 fields at the DRAO. The field spacing is 47 arcmin, which is 42 per cent of the typical Canadian Galactic Plane Survey field spacing (Taylor et al. 2003) or roughly the half power beamwidth (HPBW) of the individual antennas, explaining the enhanced sensitivity. Contrary to the Ursa Major data, these data were not filtered. The Spider DPDF survey will be further described when the remaining fields in the mosaic have been synthesized and combined with new low spatial frequency data obtained with the Green Bank 100-m telescope (Martin et al., in preparation).

The ^{12}CO ($J = 1 - 0$) and ^{13}CO ($J = 1 - 0$) data were obtained simultaneously at the 14-m FCRAO telescope with the SEcond QUabbin Optical Imaging Array (SEQUOIA) array on 2004 March 8 for the Ursa Major field and on 2005 March 2 for the Spider field. Table 2 provides the relevant parameters for each data set. The data obtained at the telescope correspond to calibrated antenna temperatures (T_A^*). To determine the main-beam temperatures (T_R^*), we divided the data by the antenna efficiency (0.45 for the ^{12}CO data and 0.48 for the ^{13}CO data). The angular resolution is 45 arcsec for the ^{12}CO ($J = 1 - 0$) data and 46 arcsec for the ^{13}CO ($J = 1 - 0$) data. The data are gridded to produce maps having 22.5 arcsec pixel^{-1} for the Spider and 20 arcsec pixel^{-1} for Ursa Major (for both species). The initial channel spacing was 0.063 km s^{-1} in the Spider and 0.066 km s^{-1} in Ursa Major while the velocity resolution is 0.077 km s^{-1} in the Spider and 0.080 km s^{-1} in Ursa Major. To increase the S/N, two successive Hanning smoothings were done on the data, resulting in a final channel spacing of $\approx$0.25 km s^{-1}. The rms noise is around 0.05 K for the ^{12}CO data and 0.02 K for the ^{13}CO data. The ^{13}CO has a lower noise amplitude because the system temperature at the ^{13}CO frequency was lower (by about a factor of 2, typically) than the system temperature at the ^{12}CO frequency.

3 RESULTS AND INTERPRETATIONS

3.1 The Spider

3.1.1 Comparison of H I and IR observations in the Spider

An approximately linear correlation exists between FIR emission and H I column density (Boulanger & Perault 1988; Boulanger et al. 1996). However, deviations from this linear correlation are often observed (Reach et al. 1998, and references therein). 'IR excess' is defined as an IR intensity larger than expected from this correlation. Under the assumption of a constant dust to gas ratio over the observed field and of constant dust properties (structure, chemical composition, size), IR excess is usually interpreted as occurring in areas where H I is optically thick or where H_2 molecules are present. Although Blitz, Bazell & Desert (1990) found no detectable CO (rms noise = 0.2 K) in the IR excess regions identified by Désert et al. (1988) where A_V is smaller than 0.25 and $N(H_2)$ is around 7.3×10^{19} cm^{-2} (UV observations), ^{12}CO (rms noise = 0.1 K) has been found in other IR excess regions (Reach et al. 1998).

The reader will have noted from Table 1 that the observed bandwidths are different for the two H I fields. This affects the data analysis (see below). As the goal of this study is mainly to find the location of the IR excess peaks, the two assumptions mentioned in the above paragraph will be used. Therefore, a similar approach must be used for the Spider and Ursa Major fields.

Table 2. Parameters of the FCRAO data cubes.

Source	Transition	Binned resolution (km s^{-1})	rms noise (T_A^*) (K)	Arcsec pixel^{-1}
Spider	^{12}CO ($J = 1 - 0$)	0.254	0.05	22.5
	^{13}CO ($J = 1 - 0$)	0.265	0.02	22.5
Ursa Major	^{12}CO ($J = 1 - 0$)	0.254	0.05	20
	^{13}CO ($J = 1 - 0$)	0.265	0.02	20

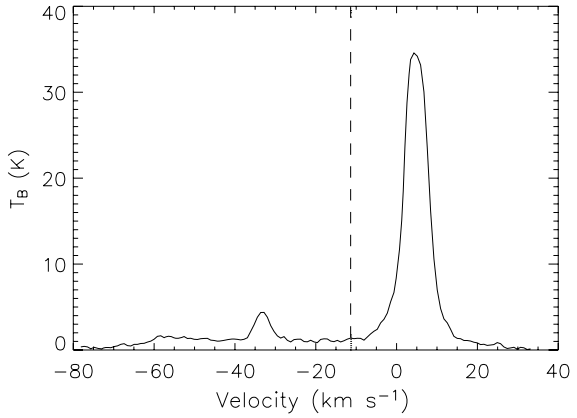

Figure 2. An H I spectrum within the Spider area ($l = 134.^{\circ}69$, $b = 40.^{\circ}49$) from DRAO data. The vertical dashed line shows the chosen separation between the local gas and the intermediate velocity gas.

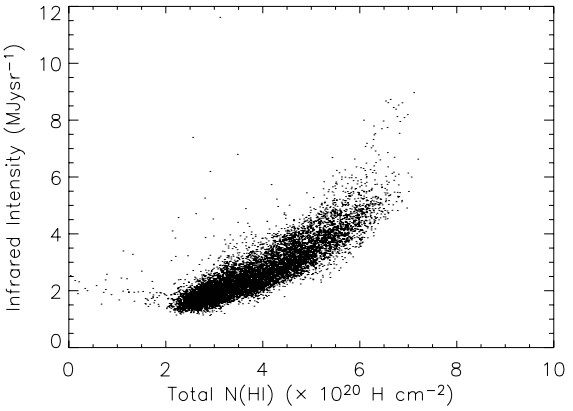

Figure 3. Plot of the FIR intensity with respect to the total H I column density ($N(\mathrm{H\,I})_{\mathrm{LVC}} + N(\mathrm{H\,I})_{\mathrm{IVC}}$) in the Spider.

The correlation between FIR intensity and H I column density is computed using 100 μm *COBE*/Diffuse Infrared Background Experiment (DIRBE) data (Hauser et al. 1998) and Leiden–Dwingeloo data (Hartmann, Magnani & Thaddeus 1998) over the whole NCL ($l = 120^{\circ}$–160°, $b = 30^{\circ}$–50°). Doing so also precludes the assumption that the gas is dominated by H I in both the Spider and Ursa Major. However, the IR and H I emission coming from the NCL is contaminated by background clouds. Fig. 2 shows an H I spectrum within the Spider area. To separate the local gas (LVC) from the intermediate velocity gas (IVC), the kinematical value of $-11.37\,\mathrm{km\,s^{-1}}$ was chosen since this is approximately half-way between the local gas peak and the intermediate velocity gas peak. A joint correlation between the 100 μm emission, the local H I gas and the intermediate velocity H I gas was then investigated, since the correlation slope could be different for the two components:

$$I_\nu = a_1\, N(\mathrm{H\,I})_{\mathrm{LVC}} + a_2\, N(\mathrm{H\,I})_{\mathrm{IVC}} + \mathrm{offset}. \quad (1)$$

The H I column density was obtained from the summed brightness temperatures. The temperatures were summed between -12.19 and $-77.31\,\mathrm{km\,s^{-1}}$ for the intermediate velocity gas and between -11.37 and $37.26\,\mathrm{km\,s^{-1}}$ for the local gas. The external limits were chosen as where no H I emission was apparent. Only data points with local H I gas column densities smaller than a threshold value ($3 \times 10^{20}\,\mathrm{cm^{-2}}$ plus the minimum column density of the field) are used to compute the correlation slope, since H_2 molecule formation is expected above this threshold (Federman, Glassgold & Kwan 1979; Gillmon et al. 2006). Table 3 provides a_1, a_2, the offset (y-intercept) and the Pearson product–moment correlation coefficient for the correlation between DIRBE and Leiden–Dwingeloo data. The offset found is similar to the cosmic FIR background ($0.78 \pm 0.21\,\mathrm{MJy\,sr^{-1}}$) determined by Lagache et al. (2000). For a 10° radius region centred on $l = 140^{\circ}$ and $b = 35^{\circ}$, Reach et al. (1998) found a slope of $0.56\,\mathrm{MJy\,sr^{-1}}/10^{20}\,\mathrm{cm^{-2}}$ and an offset of $0.63\,\mathrm{MJy\,sr^{-1}}$ for a single correlation (I_ν–N(H I)), similar to the values found here. The standard deviation of the data points with respect to the correlation for N(H I) smaller than $3.55 \times 10^{20}\,\mathrm{cm^{-2}}$ is $0.26\,\mathrm{MJy\,sr^{-1}}$, and significant deviations are identified as being larger than $+2\sigma$. This value was chosen to suppress sensitivity to the noise from the IR excess maps.

Table 3. Correlation slope parameters for the joint correlation between DIRBE and Leiden–Dwingeloo data in the NCL.

Parameter	Value
a_1 (MJy sr^{-1}/10^{20} cm^{-2})	0.536 ($\sigma = 0.008$)
a_2 (MJy sr^{-1}/10^{20} cm^{-2})	0.58 ($\sigma = 0.02$)
y-intercept (MJy sr^{-1})	+0.75
Pearson coefficient (r)	0.87

The IR excess in the Spider field was computed using the results of the joint correlation shown in Table 3 on the 100 μm IR emission map taken from the new generation of *IRAS* images (Miville-Deschênes & Lagache 2005) and our H I DRAO data. The H I DRAO data were binned to 4.3 arcmin to match the *IRAS* grid. Fig. 3 shows a plot of the FIR intensity with respect to the total H I column density ($N(\mathrm{H\,I})_{\mathrm{LVC}} + N(\mathrm{H\,I})_{\mathrm{IVC}}$). This plot shows that the IR–H I relation is linear below 3–3.5 × $10^{20}\,\mathrm{cm^{-2}}$ and curves at higher N(H I), indicating that H_2 is gradually replacing H I. Table 4 provides the parameters of the IR excess distribution above $+2\sigma$ while Fig. 4 shows a map of the IR excess computed with this method, with the contours showing the *IRAS* 100 μm emission. The IR excess peak is located at $l = 134.^{\circ}8$, $b = 40.^{\circ}4$ ($4.28\,\mathrm{MJy\,sr^{-1}}$). The IR excess is very intense ($>3\,\mathrm{MJy\,sr^{-1}}$) in the central part of the field, but more diffuse IR excess is also seen following the filamentary morphology of the H I, especially in the northern sections.

The correlation slope between the 60 μm intensity and the 100 μm intensity is 0.17 for a field which includes the Spider and Ursa Major. This correlation slope is usual for diffuse high Galactic latitude regions. An excess of 100 μm emission ($>0.5\,\mathrm{MJy\,sr^{-1}}$) with respect to this correlation is found in the IR excess region of the Spider, indicating a smaller amount of small grains as well as a possible drop in the temperature of the big grains (Abergel et al. 1996). As a low temperature is required to have molecule formation (Chang, Cuppen & Herbst 2005), this region is a potential site of H_2 formation. Although the ratio of 60 μm emission to 100 μm emission can be used to detect temperature variations, it is not possible to compute an exact temperature with this ratio. This is because the ratio is dependent both on the temperature of the big grains and

Table 4. Parameters of the IR excess distribution in the Spider.

Parameter	IR excess
Mean (MJy sr^{-1})	1.0
σ (MJy sr^{-1})	0.6
Number of points	994

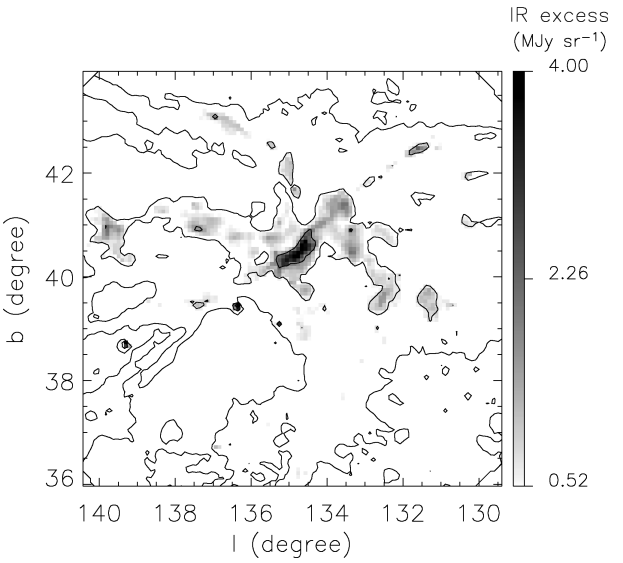

Figure 4. Map of the IR excess area in the Spider. The contours show the *IRAS* 100 μm emission (with specific contours at 2, 4 and 6 MJy sr^{-1}).

the abundance of the very small grains (Désert, Boulanger & Puget 1990).

Assuming the same 100 μm emission per H nucleus in the atomic and molecular gas (Reach et al. 1998), the IR excess map can be converted into a H_2 column density:

$$\text{IR excess} \approx a_1 2N(H_2), \quad (2)$$

where a_1 is the correlation slope between the 100 μm emission and the H I column densities (see Table 3). Table 5 provides the physical parameters inferred from the IR excess map in the Spider. To obtain a global value on the fraction of molecular gas, the total H_2 column density is computed using all data points where a positive deviation of the IR intensity with respect to the IR–H I correlation is observed. This total H_2 column density is divided by the total H I column density computed over the whole field. The ratio between H_2 and H I column densities is also computed using only the pixels with IR excess above 2σ to obtain a local value of the fraction of molecular gas. To obtain a global value of the H_2 mass, the mass is first computed from the addition of all positive pixels above the FIR–H I correlation. The H_2 mass is also computed from the addition of the pixels with IR excess above 2σ.

Table 5. Physical parameters inferred from the IR excess distribution in the Spider.

Parameter	Spider
Maximal $N(H_2)$ (10^{20} cm^{-2})	4.05
All the field	
Mean $N(H_2)$ (10^{20} cm^{-2})	0.50
Fraction of H_2[1]	0.10
H_2 Mass ($M_\odot$)	31
IR excess ($>2\sigma$)	
Mean $N(H_2)$ (10^{20} cm^{-2})	0.96
Fraction of H_2[1]	0.33
H_2 Mass ($M_\odot$)	23

[1] $2N(H_2)/(2\,N(H_2) + N(H\,I))$

3.1.2 FCRAO CO observations of the Spider

Molecular observations of the potential site of H_2 formation, described in the previous section, will now be presented. Fig. 5 shows the Spider mean H I brightness temperature maps with the contours showing the ^{12}CO integrated intensities over a similar velocity range. The velocity ranges shown for H I are where ^{12}CO is the strongest. ^{12}CO and H I clearly do not coincide. The molecular cloud is very fragmented, with weak diffuse emission around the higher density regions which extend over a few km s^{-1}. In each channel, some high-density regions disappear and other high-density regions appear.

Fig. 6 shows the ^{12}CO and ^{13}CO ($J = 1 - 0$) integrated intensity maps. The CO distributions exhibit three well-defined local maxima, which we label P1, at position (135.°13, 40.°31), P2 at (134.°80, 40.°16) and P3 at (134.°95, 39.°90). ^{13}CO is only detected in these high-density regions: P1 (0.53 K km s^{-1}), P2 (0.12 K km s^{-1}) and P3 (0.13 K km s^{-1}). The location of the third region is slightly different in ^{12}CO compared with the ^{13}CO peak (0.°03 towards smaller Galactic latitudes). Compared to ^{13}CO emission, the ^{12}CO emission is stronger by a factor of 8.5, 19.3 and 18.5 in the three regions, respectively. At the interface between two high-density regions in close proximity on the plane of the sky, the ^{12}CO profiles sometimes have two components with a velocity difference between 1.33 and 3.43 km s^{-1}. Those two components are related to two spatially superposed, but kinematically distinct, molecular features. As the number of profiles with two CO components is small (≈7 per cent), we will only use the stronger component in the following analysis.

The IR excess contours are superposed on the integrated intensity maps of Fig. 6. None of the ^{12}CO peaks coincides with the strongest IR excess peak. As the resolution of the IR data is 4.3 arcmin compared to 45 arcsec for the ^{12}CO data, the IR excess contours are unable to show any fine spatial structure. However, the absence of coincidence between both peaks is confirmed after binning the ^{12}CO data to 4.3 arcmin to match the IR excess grid. Most of the northern molecular gas coincides with larger IR excess (>1.8 MJy sr^{-1}) whereas the IR excess is generally smaller to the south (<1.8 MJy sr^{-1}).

CO data are often used to infer the properties of the molecular gas. Using the ^{12}CO and ^{13}CO data, the H_2 column densities can be estimated from two methods. In the first method, the ^{12}CO integrated intensity is multiplied by the $N(H_2)/W(CO)$ ratio (X factor). There is a large uncertainty on the X factor as it appears to vary spatially. While de Vries et al. (1987) found $X = N(H_2)/W(CO) = (0.5 \pm 0.3) \times 10^{20}$ cm^{-2} (K km s^{-1})$^{-1}$ in Ursa Major, Reach et al. (1998) measured $X = N(H_2)/W(CO) = (1.3 \pm 0.2) \times 10^{20}$ cm^{-2} (K km s^{-1})$^{-1}$ for high-latitude molecular clouds taking into account the lower dust temperature in molecular gas, a value that they found to be consistent with γ-ray determination for the same region. As we assume in Section 3.1.1 uniform dust properties over the whole NCL, $X = (0.5 \pm 0.3) \times 10^{20}$ cm^{-2} (K km s^{-1})$^{-1}$ is adopted in our study. As ^{12}CO is optically thick, the results obtained with this method are probably not completely accurate, but nevertheless according to Liszt (2007), this method gives reasonable results for diffuse clouds.

The second method is based on a number of further assumptions: (i) the gas must be in local thermodynamic equilibrium (Martin & Barrett 1978), hence the excitation temperature of the molecule (T_{ex}) equals the kinetic temperature (T_k); (ii) both ^{12}CO and ^{13}CO have the same excitation temperature; and (iii) ^{12}CO is optically thick. The latter is fulfilled here since the mean $\int T_A(^{12}CO)dv / \int T_A(^{13}CO)dv$ ratio is between 12.8 and 34.1 for our data and is smaller than the

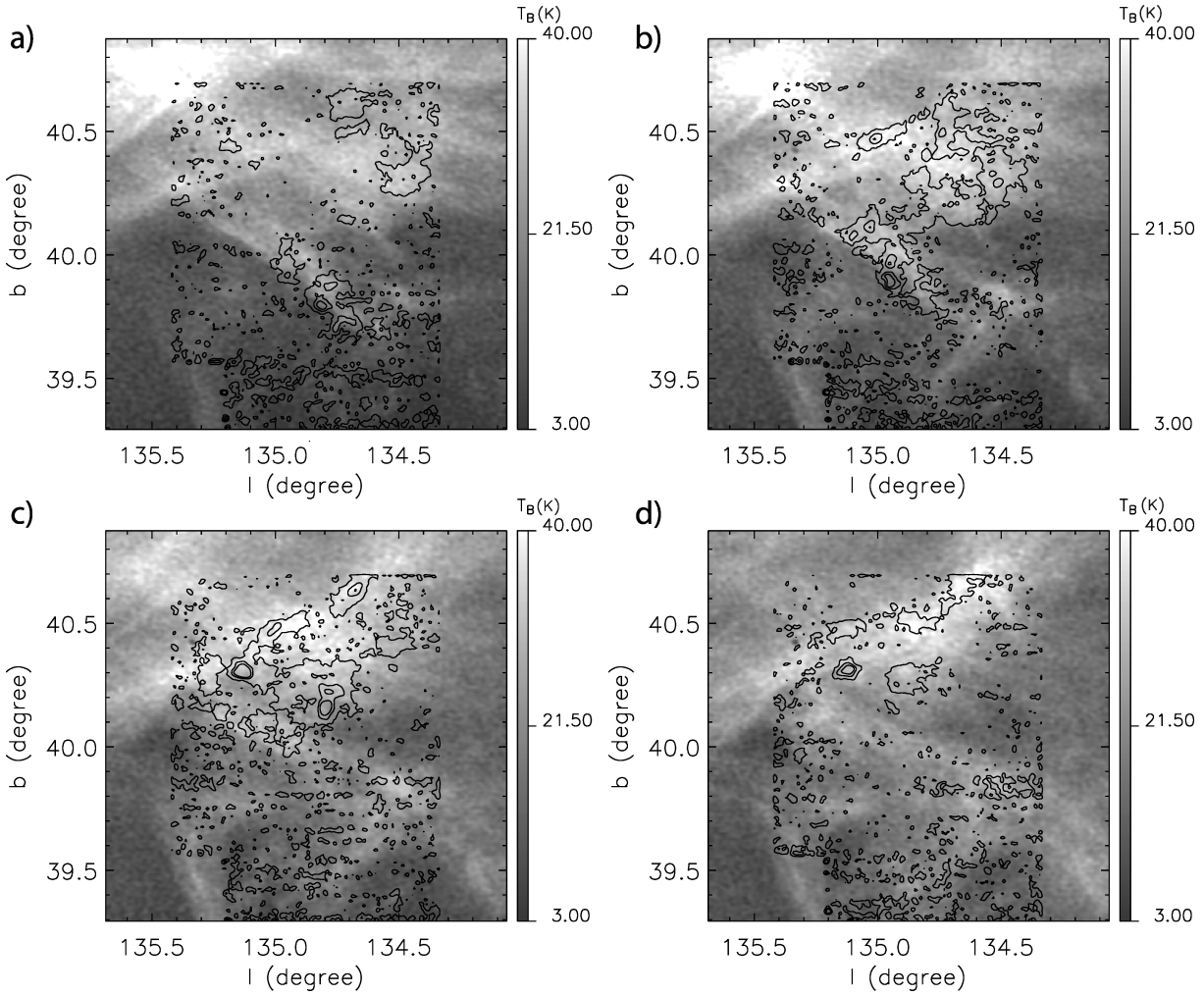

Figure 5. Spider mean H I brightness temperature grey-scale maps computed between (a) 1.90 and 2.67 km s^{-1}, (b) 2.92 and 3.68 km s^{-1}, (c) 3.94 and 4.70 km s^{-1} and (d) 4.95 and 5.71 km s^{-1}. The contours show the ^{12}CO integrated intensities over similar velocity ranges (with specific contours at 0.1, 0.5 and 1.0 K km s^{-1}). The contours to the south and at the edges do not show real emission since the noise is at least two times larger than in the field centre. The velocity ranges shown for H I are where ^{12}CO is the strongest.

relative abundances of both species (Ingalls et al. 2000). The ^{13}CO optical depth can then be calculated using (Rohlfs & Wilson 2000)

$$\tau(^{13}\mathrm{CO}) = \ln\left(1 - \frac{T_\mathrm{R}^*}{5.29}\left[\frac{1}{\exp(5.29/T_\mathrm{ex}) - 1} - 0.164\right]^{-1}\right). \quad (3)$$

The ^{13}CO column density is estimated using

$$N(^{13}\mathrm{CO}) = 2.42 \times 10^{14}\ \frac{\tau(^{13}\mathrm{CO})\,(T_\mathrm{ex} + 0.88)\,\Delta V}{1 - \exp(-5.29/T_\mathrm{ex})}, \quad (4)$$

where ΔV is the full width at half-maximum (FWHM) in km s^{-1} and T_ex and T_R^* are derived from the ^{12}CO and ^{13}CO observations, respectively. According to Dickman (1978), the ratio $N(\mathrm{H_2})/N(^{13}\mathrm{CO})$ is 7×10^5. This value was also used by Yamamoto et al. (2003) in their study of high-latitude molecular clouds, although van Dishoeck & Black (1988) states that the value could be larger in those clouds.

For small densities ($n(\mathrm{H_2}) < 750\,\mathrm{cm^{-3}}$), the ^{12}CO emission can be thermalized whereas the ^{13}CO emission is subthermally excited (Heyer et al. 2009), resulting in an overestimation of the ^{13}CO excitation temperature and an underestimation of the column density. Another possible source of error is the assumption of a constant ratio between the CO and H_2 abundances (Heyer et al. 2009) because this ratio is smaller in diffuse regions exposed to UV radiation, leading to an underestimation of the H_2 column density.

The mean H_2 column density over the field computed with the X factor method is $0.26 \times 10^{20}\,\mathrm{cm^{-2}}$ with a standard deviation of $0.20 \times 10^{20}\,\mathrm{cm^{-2}}$ and a peak H_2 column density of $2.25 \times 10^{20}\,\mathrm{cm^{-2}}$. Table 6 provides a summary of the statistical characteristics of the column density distributions for three subregions in the Spider where ^{13}CO emission was detected. The H_2 column densities computed with the method using ^{13}CO are similar to those determined with the X factor method. The H_2 column densities of the subregions 2 and 3 in the Spider are two times smaller than in subregion 1. The H I column densities found in the Spider are four times larger than the H_2 column densities, corresponding to a fraction $2N(\mathrm{H_2})/(2N(\mathrm{H_2}) + N(\mathrm{H\,I})) = 0.33$. This quantity of molecular gas is similar to the amount of IR excess as will be shown in Section 4.1.

The H_2 mass of the clouds can also be determined. Assuming a distance of 100 pc (de Vries et al. 1987), the mass (in $\mathrm{M_\odot}$) in a X arcmin $\times$ Y arcmin field with a column density $N(\mathrm{H_2})$ is given by

$$M = N(\mathrm{H_2}) \times X \times Y \times 1.36 \times 10^{-23}, \quad (5)$$

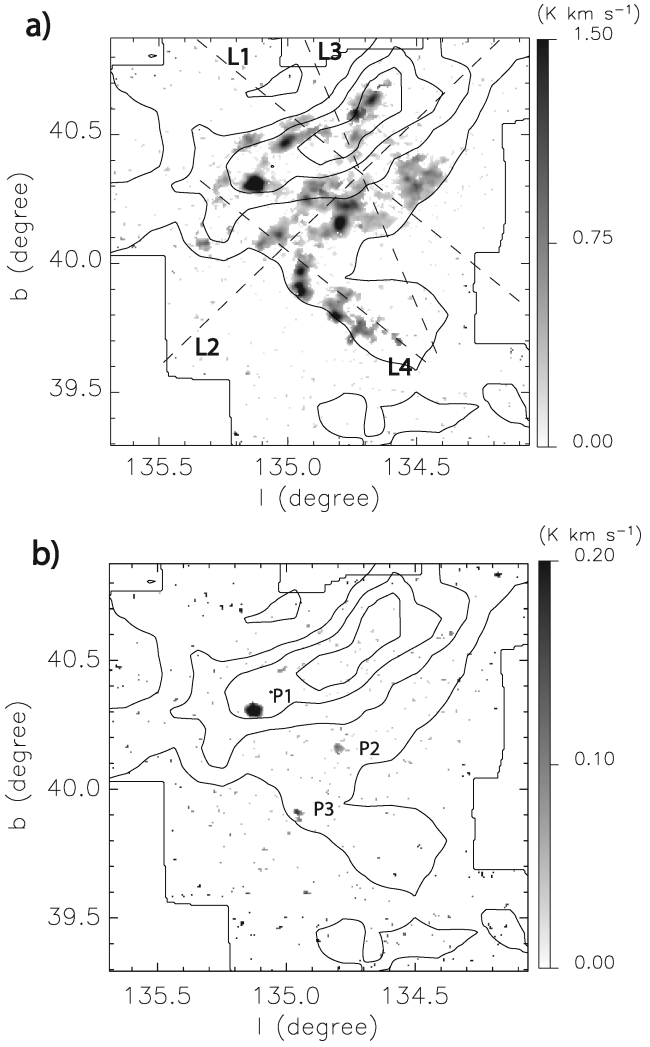

Figure 6. (a) ^{12}CO integrated intensity map for the Spider in grey-scale. The four dashed lines (L1, L2, L3 and L4) show the directions along which position–velocity cuts will be later drawn. (b) ^{13}CO integrated intensity map for the Spider. ^{13}CO is observed in three regions identified as P1, P2 and P3. The contours show the IR excess in the Spider maps (with specific contours at 0.52, 1.52, 2.52 and 3.52 MJy sr^{-1}). The limits of the ^{12}CO and ^{13}CO maps are also shown.

where the last term is a factor of conversion between arcmin and cm^{-2} multiplied by the mass of an H_2 molecule. The total H_2 mass of the Spider derived using ^{12}CO is only 0.3 $M_\odot$. The mass located in regions where ^{12}CO is observed without ^{13}CO detection represents 89 per cent of the total mass.

In summary, the results of this section clearly show that although there is a correlation between IR excess and CO emission, at a detailed level there is a discrepancy between the position of the IR excess peak and the ^{12}CO peaks in the Spider. The Spider ^{12}CO emission is fragmented into about 15 high-density regions, but ^{13}CO is detected only in three of these regions.

3.1.3 Comparison of the H I and CO observations in the Spider

We will now compare the ^{12}CO observations described in the previous section with the DRAO H I data. This comparison will provide valuable information about the H I–H_2 transition. We remind the reader that the angular resolution is 1 arcmin for the H I data with 18 arcsec pixel^{-1} and the angular resolution is 45 arcsec for the ^{12}CO data with 22.5 arcsec pixel^{-1}. To increase the S/N, the H I data were spatially binned by a factor of 3, resulting in a grid with 54 arcsec pixel^{-1}. To compare both lines, the ^{12}CO data were also binned to 54 arcsec pixel^{-1} to match the H I grid.

The ^{12}CO profiles were fitted with one or two Gaussian components as needed to determine the kinematical behaviour of the molecular gas. Note that in this paper, all radial velocities are expressed with respect to the Local Standard of Rest (LSR). In general, the velocity does not vary significantly within one high-density region. The molecular gas to the north and at small Galactic longitudes (see Fig. 6) is more redshifted ($\approx$5 km s^{-1}) than the molecular gas to the south and at larger Galactic longitudes ($\approx$2 km s^{-1}) with respect to the mean velocity.

The H I profiles observed in the Spider are very complex. To better understand the nature of the observed H I emission, we have decomposed the spectra into a sum of Gaussians. This enables us to differentiate the signal coming from the warm neutral medium (broad Gaussians) and the cold neutral medium (narrow Gaussians). However, a Gaussian decomposition is known for its lack of a unique solution and its subjectivity (Haud 2000; Heiles & Troland 2003). We have reduced these problems by developing a robust technique to decompose the H I spectra into a sum of Gaussian components, using both a genetic algorithm (GA; Charbonneau 1995) as well as least-squares minimization based on the Levenberg–Marquardt technique (LM; Markwardt 2009).

The GA is a class of stochastic search algorithms which performs a directional search of the entire parameter space in order to (in our case) find the best combination of Gaussians to reproduce the spectra. Each Gaussian is defined by three parameters (amplitude, velocity and width), so the GA starts with a 'population' of random solutions. The fittest individuals, defined as those with the smallest reduced χ^2 goodness of fit are combined to form new 'child' solutions which form a new 'generation'. Individual Gaussian components may also be removed by the GA if they result in a lower value of the reduced χ^2. This new generation is then subject

Table 6. Statistical parameters of the density distributions in the Spider.

Parameter	P1	P2	P3
Mean N(H I) (10^{20} cm^{-2})	4.87 ± 0.03	4.04 ± 0.04	3.83 ± 0.04
Mean $N(H_2)$ (X-factor) (10^{20} cm^{-2})	1.22 ± 0.07	0.87 ± 0.04	0.79 ± 0.04
Mean $N(H_2)$ (^{13}CO method) (10^{20} cm^{-2})	1.50 ± 0.08	0.57 ± 0.02	0.80 ± 0.04
H_2 Mass (X-factor) ($M_\odot$)	0.022	0.0057	0.0046
H_2 Mass (^{13}CO method) ($M_\odot$)	0.027	0.0033	0.0044
^{12}CO S/N ratio	13.9–72.0	29.1–55.5	14.4–32.9
^{13}CO S/N ratio	3.4–32.7	3.4–7.4	3.0–5.7
Number of points	94	32	30

to random 'mutation' whereby each digit of each parameter has a probability of being replaced by a random number. This combination and mutation of solutions is allowed to carry on for a fixed number of generations. This best guess is then supplied to a more traditional least-squares minimization routine which provides much faster convergence, but which, without the GA's help, is more likely to fall into a local minimum.

Thus far, each spectrum has been fitted independently of its neighbours. However, there should be some continuity in a particular component from one pixel to the next, as we are not expecting a strong Gaussian component to disappear or appear too quickly. To ensure this continuity, each pixel is subjected to a second decomposition, where the initial guess used is the median of neighbours' solutions. This triple approach (GA, LM and spatial smoothing) reduces the subjectivity and non-uniqueness of the fitting procedure. We are thus able to reliably determine the column density and the velocity as well as the velocity dispersion of the different ISM phases.

Depending on the location, the H I spectra always have one or two narrow components, whereas a broad component (BC) is needed to fit the H I blueshifted emission. Fig. 7 shows an example of Gaussians fitted to H I and ^{12}CO profiles in the Spider. We remind the reader that the channel spacing of the CO data is better by a factor of 3 compared to H I (see Tables 1 and 2). The main peak of the H I profile coincides with the CO profile. The H I narrow component 2 (NC2, dotted line) is probably physically related to

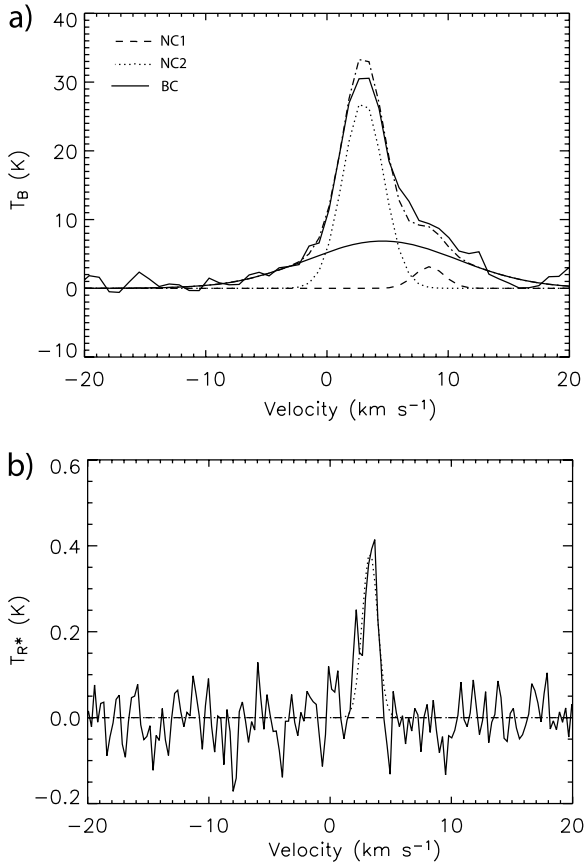

Figure 7. (a) An H I profile within the Spider area (134.°45, 40.°31) with three fitted Gaussians. The dash–dot line represents the resulting combined fit. (b) ^{12}CO profile with the fitted Gaussian at the same location as the H I profile (NC2 in particular).

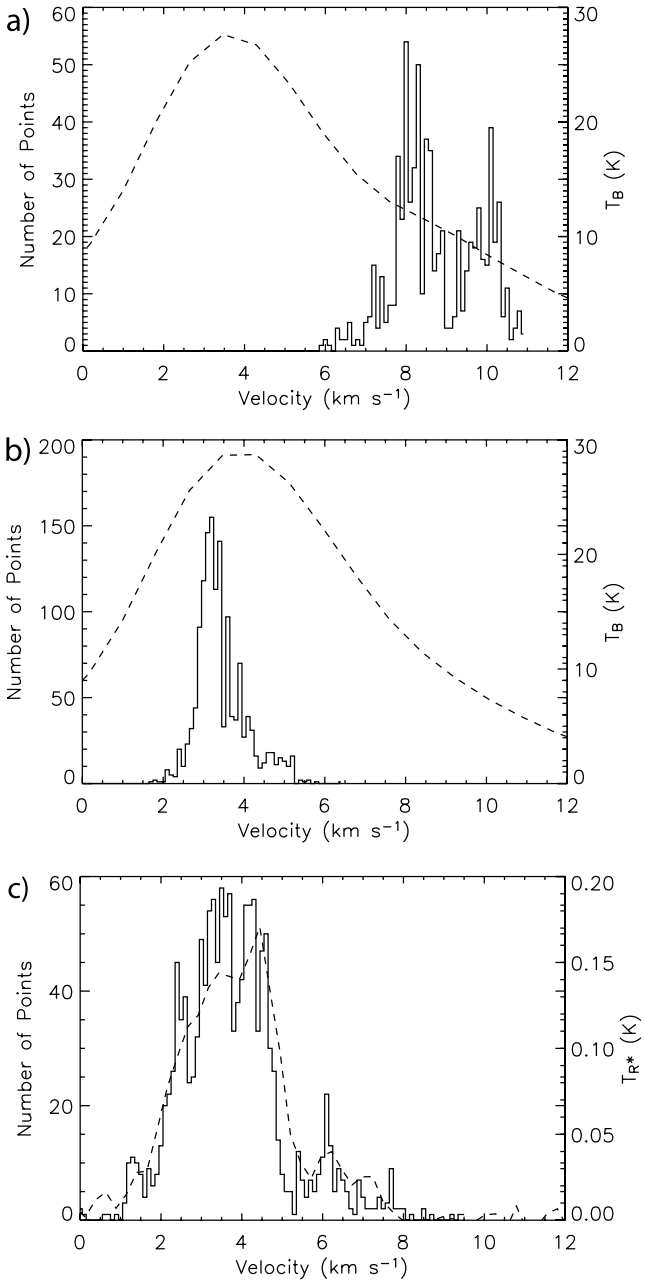

Figure 8. (a) H I NC1 velocity histogram in the Spider for the 713 pixels where ^{12}CO was detected and where H I NC1 is observed. The dashed line (right axis) shows the average H I spectrum for these pixels. (b) H I NC2 velocity histogram in the Spider for the 1433 pixels where ^{12}CO was detected. The dashed line (right axis) shows the average H I spectrum for these pixels. (c) ^{12}CO velocity histogram in the Spider. The dashed line (right axis) shows the average ^{12}CO spectrum. See Section 3.1.3 for explanations.

the ^{12}CO. The other components of the H I profile are the narrow component 1 (NC1, dashed line) and the BC (solid line).

Figs 8(a)–(c) show the histograms of the central velocities of the two narrow H I components and the ^{12}CO component for the pixels where there is a ^{12}CO detection. The H I and ^{12}CO average spectra for these pixels are also plotted (dashed line). Table 7 lists the statistics of the NC1, NC2 and ^{12}CO central velocity distributions. The two narrow H I components were separated according to their velocities, explaining the absence of overlap between both distributions. The mean difference between the ^{12}CO and H I NC1

Table 7. Statistical parameters of the ^{12}CO and H I central velocity distributions in the Spider.

Component	Mean velocity (km s^{-1})	Standard deviation (km s^{-1})
H I NC1	8.84 ± 0.04	1.07 ± 0.03
H I NC2	3.49 ± 0.03	0.62 ± 0.01
^{12}CO	3.84 ± 0.03	1.33 ± 0.02
Component	Mean line width (σ) (km s^{-1})	Standard deviation (km s^{-1})
H I NC1	1.50 ± 0.02	0.61 ± 0.02
H I NC2	2.18 ± 0.01	0.381 ± 0.007
^{12}CO	0.409 ± 0.004	0.170 ± 0.004

velocities is -5.40 ± 0.06 km s^{-1}, whereas the mean H I NC2 velocity is more blueshifted than the mean ^{12}CO velocity by only 0.35 ± 0.04 km s^{-1}. The standard deviation of the H I NC2 histogram is two times smaller than for the ^{12}CO histogram, indicating that the H I velocity is varying less than the ^{12}CO velocity. This is the result of the high-density CO regions to the north and to the south which are moving with velocities smaller or larger compared to the mean ^{12}CO velocity and which are probably not related to H I NC2. The ^{12}CO velocity distribution is skewed by a secondary bump caused by three high-density regions further north.

Fig. 9 shows H I and ^{12}CO position–velocity cuts and the IR excess profiles along the L1 and L2 lines shown in Fig. 6. Along L1, the ^{12}CO emission is located in a region where the H I NC1 component becomes weaker and the H I NC2 component appears, confirming the relation between NC2 and ^{12}CO. Much of the ^{12}CO emission is located in a region where H I linewidths are larger than elsewhere ($\approx$7 km s^{-1}). In such regions, H I velocity-shears are observed and they will be used rather than velocity gradients since the projection of the measured velocity (line-of-sight velocity) is perpendicular to the plane of the sky. Note that due to the geometry, a gradient on the line of sight does not necessarily imply a shear. The values of the H I velocity-shears are estimated by eye. We compute the velocity difference between two high brightness H I features as seen on the plot and we divide it by the angular offset. The value is approximate and the uncertainty is at most 25 per cent. A change of $\approx$9 km s^{-1} is observed over $\approx$7 arcmin, corresponding to an H I velocity-shear of 44 km s^{-1} pc^{-1} between L1-a and L1-b. Between L1-b and L1-c, the H I velocity-shear is 18 km s^{-1} pc^{-1}, two times smaller. The H I velocity-shear positions coincide with ^{12}CO emission. Along L2, the ^{12}CO emission is located where NC2 becomes dominant, but the presence of a velocity-shear is not obvious.

Fig. 10 shows H I and ^{12}CO position–velocity cuts and the IR excess profiles along the L3 and L4 lines shown in Fig. 6. The L3 line goes through the IR excess peak, shown in Fig. 10c. Between L3-b and L3-c, a small H I velocity-shear is observed ($\approx$10 km s^{-1} pc^{-1}). At the location of the IR excess peak, the H I velocity line width is larger ($\approx$8 km s^{-1}) than anywhere, whereas the ^{12}CO emission is modest (maximum = 0.46 K, width $\approx$ 0.5 km s^{-1}) compared to the integrated intensities found at other locations. More cuts were made along different directions and in the vicinity of the IR excess peak. A large H I velocity-shear ($\approx$29 km s^{-1} pc^{-1} between L3-a and L3-b) is observed in each direction, except along the line going from the south ($l = 135\overset{\circ}{.}48, b = 40\overset{\circ}{.}10$) to the north ($l = 134\overset{\circ}{.}01, b = 40\overset{\circ}{.}83$). This H I velocity-shear is observed in a region with a radius of about 5 arcmin.

Along L4, there is a correlation between the ^{12}CO gas and enhancement of the H I brightness temperature of NC2. A H I velocity-shear ($\approx$20 km s^{-1} pc^{-1}) is observed between L4-a and L4-b, while larger velocity-shears (>20 km s^{-1} pc^{-1}) are observed along a line perpendicular to this direction (not shown in the figure). Moreover, along L4, the ^{12}CO emission located near $l = 134\overset{\circ}{.}88$ and $b = 39\overset{\circ}{.}96$ is where the more diffuse second H I component (NC1) becomes weaker.

Looking now at the line widths, Fig. 11 shows a scatter plot of the second moment of all the H I line profiles versus the ^{12}CO line integrated intensity. The histogram shows the number of H I profiles in each bin of 0.2 km s^{-1} for the H I second moment. Where there is no detectable ^{12}CO, the H I second moment reaches $\approx$6.6 km s^{-1}, whereas it is smaller than $\approx$5.5 km s^{-1} where ^{12}CO is detected. The low-intensity ^{12}CO regions therefore have H I line widths extending to higher values than for the bulk of the ^{12}CO. The average of the H I second moment is around 4.3 km s^{-1} where W(CO) is larger than 3 K km s^{-1}, in the P1 region (Fig. 6).

Other cuts were made through the northern region where the molecular gas is moving with velocities $\approx$6 km s^{-1} or through the southern region where the molecular gas is moving with velocities $\approx$2 km s^{-1}, but the locations of those regions do not coincide with significant H I velocity-shears. Velocity-shears are mostly observed in the central regions where the molecular gas is moving with the same velocity as the H I gas ($\approx$4 km s^{-1}).

In summary, the coincidence between ^{12}CO velocities and the NC2 H I velocities in the Spider was shown. Where ^{12}CO appears, there usually are large H I velocity-shears or the merging of two H I components. The strength of the CO emission does not scale with the magnitude of the velocity-shear.

3.2 Ursa Major

3.2.1 Comparison of H I and IR observations in Ursa Major

Contrary to the Spider, information on the IVC clouds is not available in the Ursa Major due to the spectrometer's limited number of channels at the time of the observations. H I DRAO column densities are therefore lower limits in Ursa Major. The single correlation between the FIR intensity and the H I column density (between -7.00 and 18.95 km s^{-1} which is the velocity range of our DRAO data) was therefore computed using *COBE*/DIRBE and Leiden–Dwingeloo data over the NCL ($l = 120°$–$160°, b = 30°$–$50°$). The program SLOPES was used to compute the ordinary least-squares (OLS) regression (Isobe et al. 1990; Feigelson & Babu 1992). Table 8 provides the slope, the offset (y-intercept) and the Pearson product–moment correlation coefficient for this correlation. The offset is larger than for the joint correlation computed in the Spider since IR emission is associated with the IVC clouds. The standard deviation of the data points with respect to the correlation for N(H I) smaller than 3.55×10^{20} cm^{-2} is 0.3 MJy sr^{-1}, and significant deviations are identified as being larger than 2σ.

The IR excess was computed the same way as for the Spider area. Fig. 12 shows a plot of the FIR intensity with respect to the local H I column density. There are two superposed components. The first component (the points at the bottom of the plot) is defined by small IR intensities for all N(H I) and is probably related to another cloud. A non-linear increase of the IR intensity with the H I column density is observed for the second component for N(H I) larger than $\approx 3 \times 10^{20}$ cm^{-2}. Table 9 provides the parameters of the IR excess distribution and a map of the IR excess is shown in Fig. 13, with contours showing the *IRAS* 100 μm emission. Three regions show

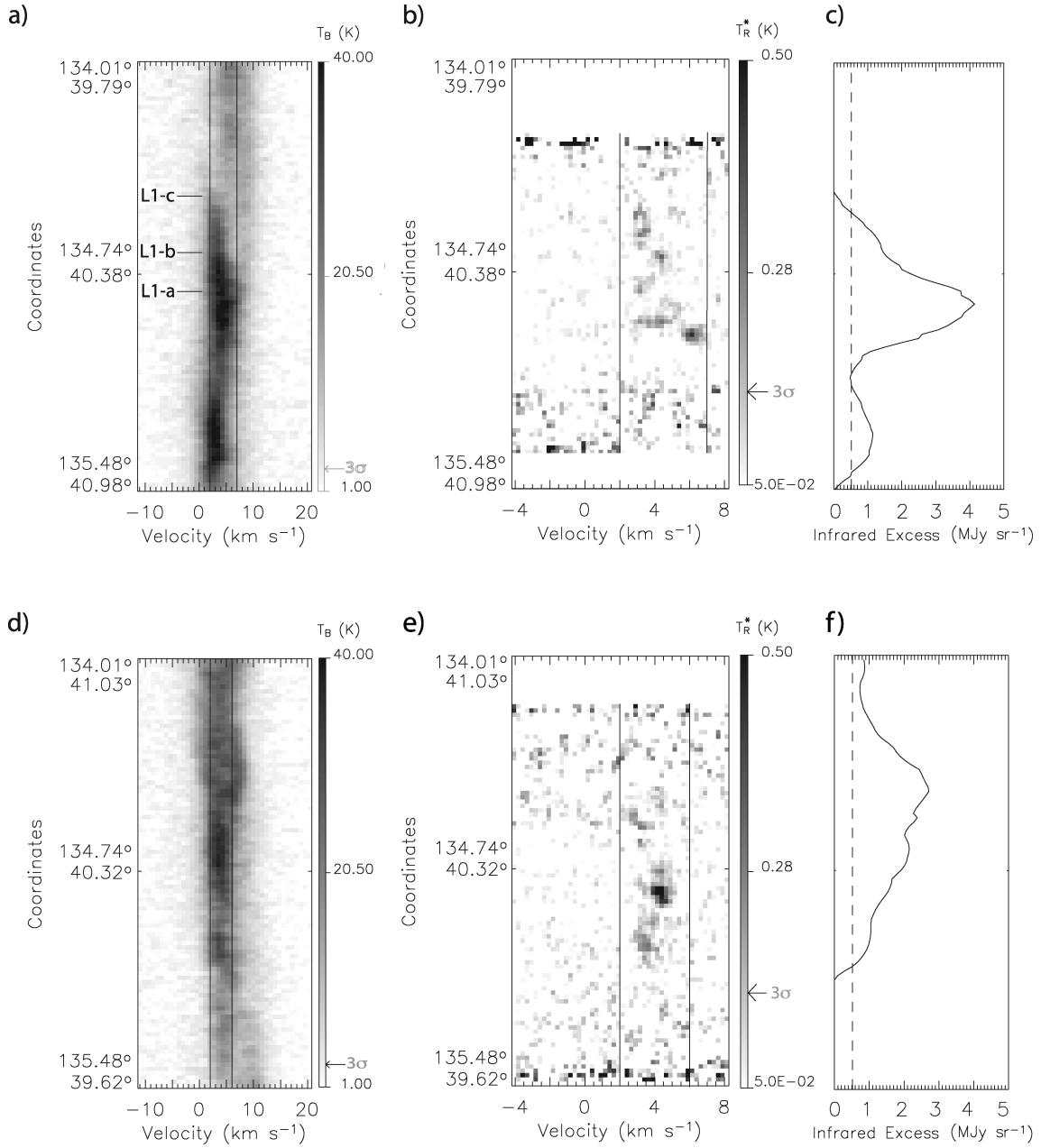

Figure 9. (a) H I position–velocity plot in the Spider along line L1 of Fig. 6. (b) ^{12}CO position–velocity plot along the same cut as in (a). (c) IR excess profile along line L1. (d) H I position–velocity plot in the Spider along line L2 of Fig. 6. (e) ^{12}CO position–velocity plot along the same cut as in (d). (f) IR excess profile along line L2. The two vertical lines show the range of the ^{12}CO velocities which is narrower than the range of the H I velocities as defined in Fig. 7 (compare the same lines in the left-hand panels). All emission above the noise is plotted and the 3σ threshold is shown on the plot scale. The dashed vertical line on the IR excess profile shows the 2σ threshold.

intense IR excess and diffuse IR excess is present between those regions. The IR excess peak of the northern region, observed in ^{12}CO in this study, is located at $l = 140.^{\circ}77$, $b = 39.^{\circ}74$ (and has a value of 6.33 MJy sr^{-1}).

Using the same method as in Section 3.1.1, the H_2 column densities and masses were inferred from the IR excess map. Only upper limits for the H_2 column density are obtained since the contribution from IVC gas was not subtracted from the IR excess. Table 10 provides the physical parameters inferred from the IR excess map in Ursa Major.

3.2.2 *FCRAO CO observations of Ursa Major*

As for the Spider area, the location of the IR excess peak discovered in the previous section is a potential site of H_2 formation. Fig. 14 shows the mean H I brightness temperature maps and the contours show the ^{12}CO integrated intensities over a similar velocity range. The velocity ranges shown for H I are where ^{12}CO is strongest. There is no one-to-one coincidence between H I and ^{12}CO emission. The ^{12}CO emission is fragmented in many high-density regions but located in a medium with strong diffuse emission. The morphology

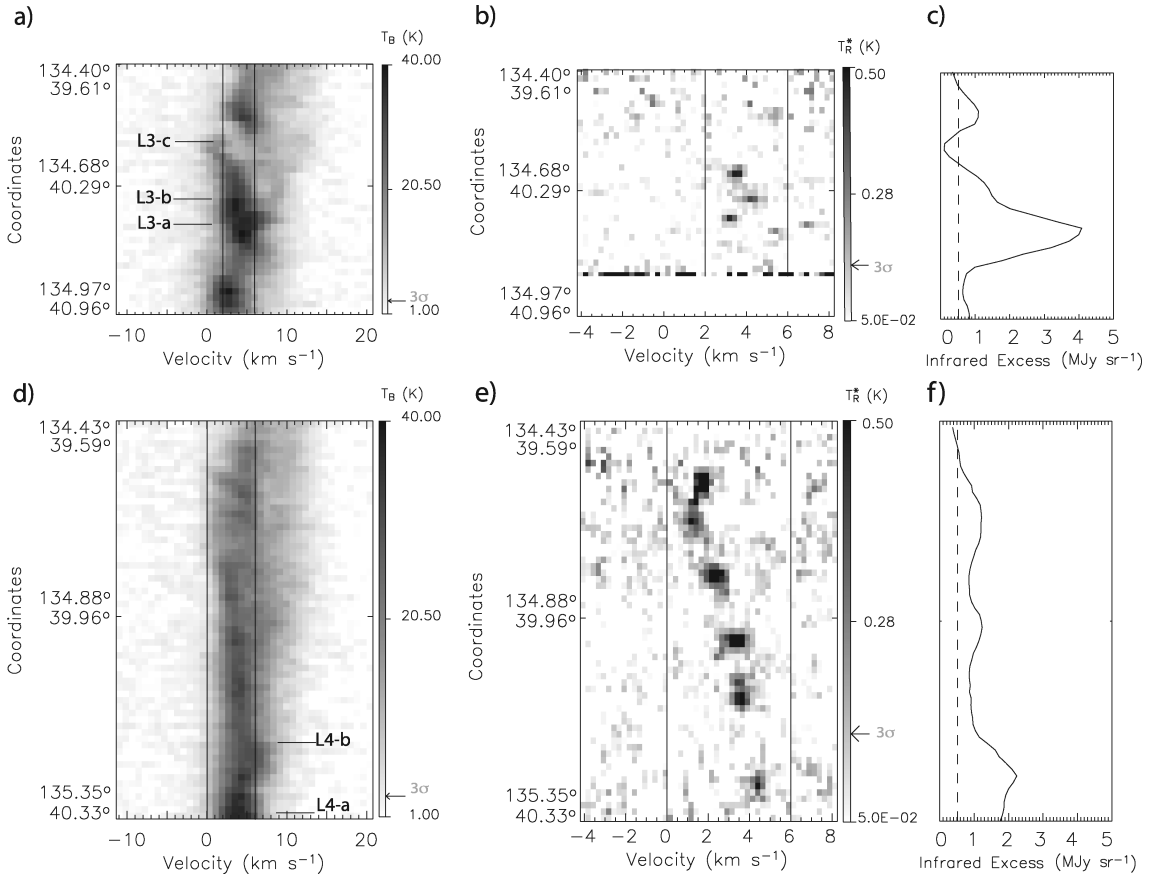

Figure 10. (a) H I position–velocity plot in the Spider along line L3 of Fig. 6. (b) ^{12}CO position–velocity plot along the same cut as in (a). (c) IR excess profile along line L3. (d) H I position–velocity plot in the Spider along line L4 of Fig. 6. (e) ^{12}CO position–velocity plot along the same cut as in (d). (f) IR excess profile along line L4. Lines are as in Fig. 9.

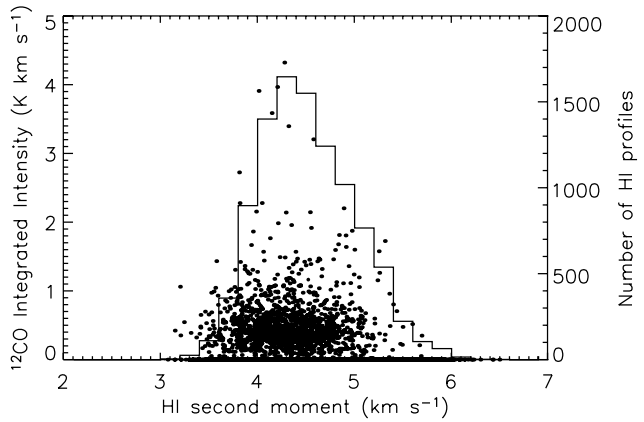

Figure 11. Scatter plot of the ^{12}CO line integrated intensity and the second moment of all H I line profiles. The histogram (right axis) shows the number of H I profiles in each bin of 0.2 km s^{-1} for the H I second moment.

of Ursa Major is therefore similar to typical molecular clouds. At this resolution, some high-density regions seem to be superposed and they are visible in almost all the channels shown in Fig. 14.

Fig. 15 shows the ^{12}CO and ^{13}CO ($J = 1 - 0$) integrated intensity maps. The ^{12}CO peak is located to the south at small Galactic longitudes (6.7 K km s^{-1}) and the northern ^{12}CO emission at larger Galactic longitude is more diffuse (maximum $\approx$ 1.9 K km s^{-1}). Some diffuse emission is separated from the central region. Detection of ^{13}CO occurs only in three juxtaposed, but distinct regions, with maximal integrated intensities between 0.3 and 0.6 K km s^{-1}. The mean $\int T_A(^{12}\mathrm{CO})\mathrm{d}v / \int T_A(^{13}\mathrm{CO})\mathrm{d}v$ ratio is lower than 12.

Table 8. Correlation slope parameters for a single correlation between DIRBE and Leiden–Dwingeloo data in the NCL.

Parameter	Value
Slope (MJy sr^{-1}/10^{20} cm^{-2})	0.62 ($\sigma = 0.01$)
y-intercept (MJy sr^{-1})	+1.13 ($\sigma = 0.01$)
Pearson coefficient (r)	0.82

The IR excess contours are superposed on the integrated intensity maps in Fig. 15. The IR excess peak is located in a region where ^{12}CO emission is diffuse. As the resolution of the IR data is 4.3 arcmin compared to 45 arcsec for the ^{12}CO data, the IR excess contours are unable to show any fine spatial structure. As in the Spider, the absence of coincidence between both peaks is confirmed after binning the ^{12}CO data to 4.3 arcmin to match the IR excess grid. Significant IR excess ($> 2\sigma$) is present over the whole molecular cloud. No ^{12}CO is detected to the north and at large Galactic longitudes where IR excess is still observed.

The H_2 column densities were computed using the methods discussed in Section 3.1.2. The mean H_2 column density over the field computed with the X factor method is 0.57×10^{20} cm^{-2} with a standard deviation of 0.49×10^{20} cm^{-2} and a peak H_2 column density

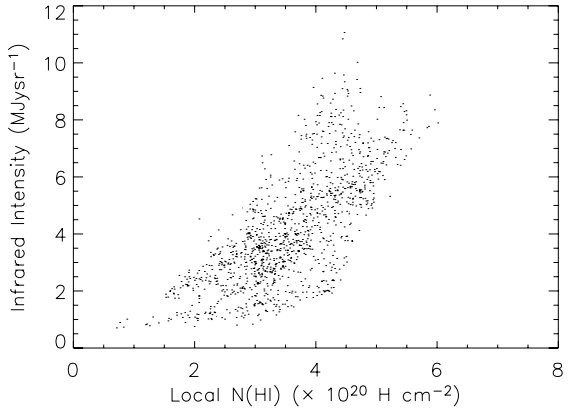

Figure 12. Plot of the FIR intensity with respect to the local H I column density in Ursa Major. The cosmic FIR background (0.78 ± 0.21 MJy sr^{-1}) was subtracted from the 100 μm intensity in this plot.

Table 9. Parameters of the IR excess distribution in Ursa Major.

Parameter	IR excess
Mean (MJy sr^{-1})	2.3
σ (MJy sr^{-1})	1.3
Number of points	858

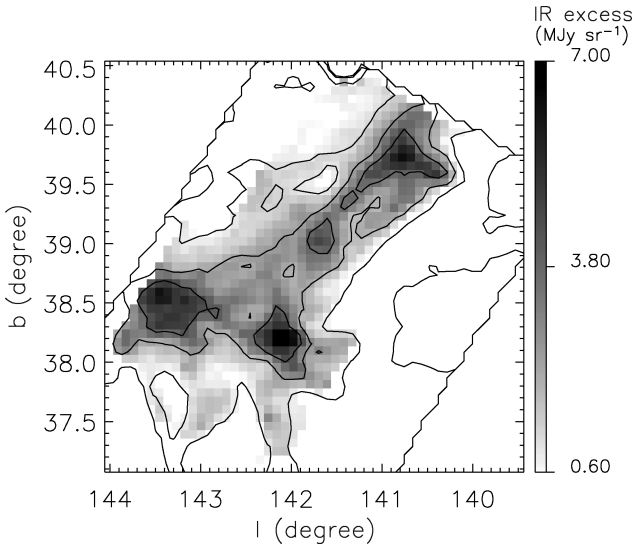

Figure 13. Map of the IR excess area in Ursa Major. The contours show the *IRAS* 100 μm emission (with specific contours at 2, 4, 6 and 8 MJy sr^{-1}).

of 3.33×10^{20} cm^{-2}. Table 11 provides a summary of the statistical characteristics of the column density distributions in Ursa Major for regions where ^{13}CO emission was detected. The H_2 column density found with the *X* factor method are three times smaller than the amount of H I. The total H_2 mass for Ursa Major derived using ^{12}CO only is 0.32 $M_\odot$. The mass located in regions where ^{12}CO is observed without a ^{13}CO detection accounts for 72 per cent of the total mass.

3.2.3 Comparison of the H I and CO observations in Ursa Major

We remind the reader that the angular resolution is 1 arcmin for the H I data with 30 arcsec pixel^{-1} and the angular resolution is 45 arcsec for the ^{12}CO data with 20 arcsec pixel^{-1}. To compare both lines, the ^{12}CO data were binned to 30 arcsec pixel^{-1} to match the H I grid. Using the Gaussian fitting method described in Section 3.1.3, the ^{12}CO, ^{13}CO and H I velocities were determined across the region. There is a weak ^{12}CO velocity gradient from the north at large Galactic longitude (8 km s^{-1}) to the south at small Galactic longitude (6.5 km s^{-1}). Fig. 16 shows an example of Gaussians fitted to H I and ^{12}CO profiles. The channel spacing of the CO data is better by a factor 3 compared to H I (see Tables 1 and 2). The ^{12}CO profile is coincident with the redshifted part of the H I profile. The NC1 (dashed line) is the closest to the ^{12}CO line, whereas the NC2 (dotted line) is blueshifted with respect to NC1. The dash–dot line shows the H I BC.

Table 10. Physical parameters inferred from the IR excess distribution in Ursa Major.

Parameter	Ursa Major
Maximal $N(H_2)$ (10^{20} cm^{-2})	5.46
All the field	
Mean $N(H_2)$ (10^{20} cm^{-2})	1.61
Fraction of H_2[1]	0.43
H_2 Mass ($M_\odot$)	39
IR excess ($>2\sigma$)	
Mean $N(H_2)$ (10^{20} cm^{-2})	1.84
Fraction of H_2[1]	0.50
H_2 Mass ($M_\odot$)	38

[1] $2N(H_2)/(2N(H_2) + N(H\,I))$

Fig. 17 shows the histograms of the central velocities of the two narrow H I components and the ^{12}CO component for the pixels where there is a ^{12}CO detection. The H I and ^{12}CO average spectra for these pixels are also plotted (dashed line). Table 12 lists the statistics of the NC1, NC2 and ^{12}CO central velocity distributions. The S/N of the Ursa Major H I profiles before filtering is smaller than for the Spider H I profiles, resulting in a poorer Gaussian fit in several cases. As it is impossible to systematically look at each profile individually, the statistical parameters should give a good idea of the H I kinematical behaviour in Ursa Major, keeping in mind the limitations of the Gaussian fitting programme for those noisy spectra. The histogram peaks do not coincide, indicating that the molecules are kinematically distinct from the H I in this field. The mean difference between the ^{12}CO and H I NC1 velocities is 1.67 ± 0.03 km s^{-1} compared to 5.34 ± 0.04 km s^{-1} for the mean velocity difference between ^{12}CO and H I NC2.

Fig. 18 shows H I and ^{12}CO position–velocity cuts and the IR excess profiles along the lines shown in Fig. 15. Along L5, which goes through the ^{12}CO emission peak region, H I emission surrounds the ^{12}CO emission. The H I velocity-shear varies from 16 km s^{-1} pc^{-1} between L5-a and L5-b to 13 km s^{-1} pc^{-1} between L5-b and L5-c. Along L6 ^{12}CO and H I have a similar kinematical behaviour since the ^{12}CO and H I plots have approximately the same shape along this position–velocity cut. ^{12}CO emission appears near L6-a, where IR excess is observed and where two H I components merge into one component. Between L6-a and L6-b, an H I velocity-shear of 54 km s^{-1} pc^{-1} is observed and a smaller H I velocity-shear of 17 km s^{-1} pc^{-1} is observed between L6-c and L6-d. Another cut was done in a perpendicular direction through the IR excess and this is shown in Fig. 18(g). Along L7, an H I velocity-shear of 19 km s^{-1} pc^{-1} is observed at the location of the IR excess between

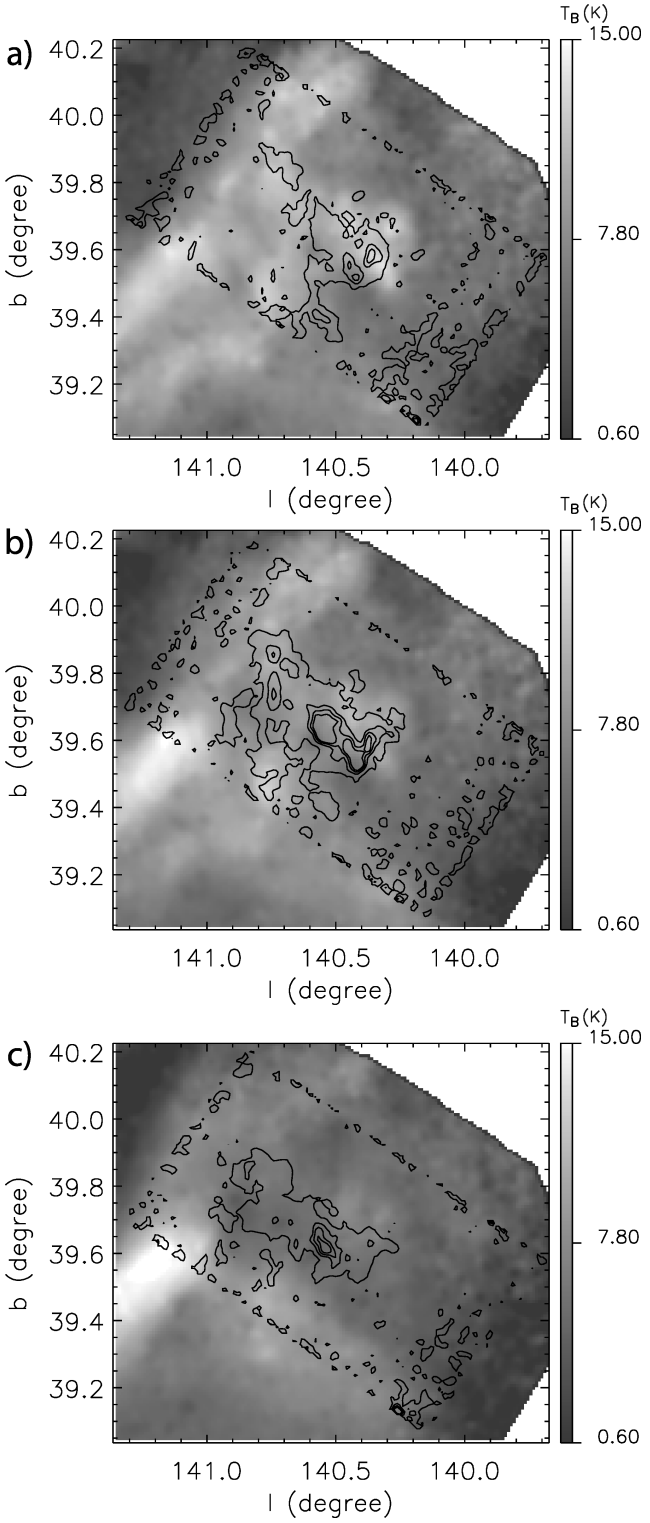

Figure 14. Ursa Major mean H I brightness temperature grey-scale maps computed between (a) 6.04 and 6.80 km s^{-1}, (b) 7.05 and 7.82 km s^{-1} and (c) 8.07 and 8.83 km s^{-1}. The contours show the ^{12}CO integrated intensities over similar velocity ranges (with specific contours at 0.15, 0.65, 1.15 and 1.65 K km s^{-1}). The contours to the south and at the edges do not show real emission since the noise is at least two times larger than in the field centre. The velocity ranges shown for H I are where ^{12}CO is strongest.

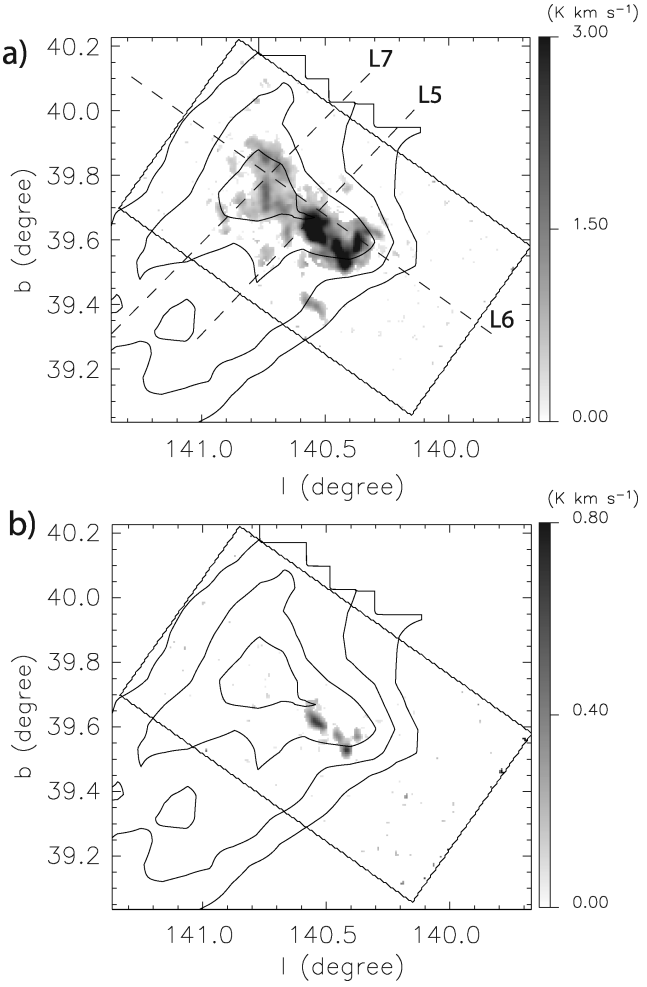

Figure 15. (a) ^{12}CO integrated intensity map for Ursa Major in grey-scale. The three dashed lines (L5, L6 and L7) show the cuts along which position–velocity plots will later be drawn. (b) ^{13}CO integrated intensity map for Ursa Major. The contours show the IR excess in the Ursa Major maps (with specific contours at 0.6, 2.1, 3.6 and 5.1 MJy sr^{-1}). The limits of the ^{12}CO and ^{13}CO maps are also shown.

Table 11. Statistical parameters of the density distributions in Ursa Major where ^{13}CO is detected.

Parameter	Ursa Major
Mean N(H I) (10^{20} cm^{-2})	4.76 ± 0.02
Mean $N(H_2)$ (X-factor) (10^{20} cm^{-2})	1.72 ± 0.04
Mean $N(H_2)$ (^{13}CO method) (10^{20} cm^{-2})	1.8 ± 0.05
H_2 Mass (X-factor) ($M_\odot$)	0.09
H_2 Mass (^{13}CO method) ($M_\odot$)	0.1
^{12}CO S/N ratio	3.4–63.7
^{13}CO S/N ratio	3.0–23.8
Number of points	346

L7-b and L7-c. The ^{12}CO emission is mainly associated with the diffuse H I component. There is a larger H I velocity-shear of 30 km s^{-1} pc^{-1} between L7-a and L7-b, but the corresponding ^{12}CO emission is weaker. Along this cut, the main H I component changes from ≈8 to ≈3 km s^{-1}.

Other cuts not shown in the figure were also made. A velocity-shear of ≈16 km s^{-1} is observed along another cut parallel to L6 where IR excess is found, but where CO is not detected. However,

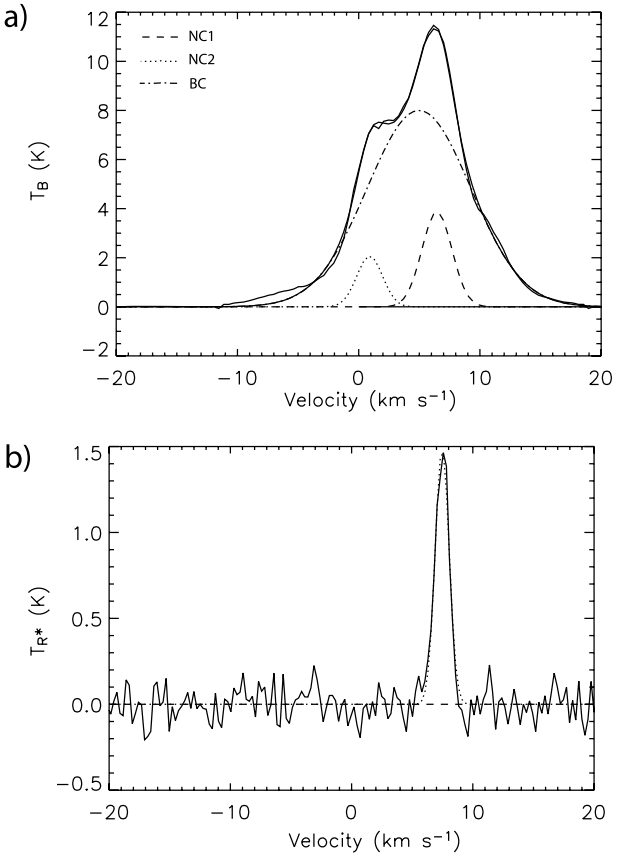

Figure 16. (a) An H I profile within the Ursa Major area (140.°51, 39.°67) with three fitted Gaussians. The solid line shows the resulting fit. (b) ^{12}CO profile with the fitted Gaussian at the same location as the H I profile.

no velocity-shear is observed on a cut parallel to L5, where no IR excess is found.

In summary, the H I velocity is usually blueshifted with respect to the ^{12}CO velocity in Ursa Major. Compared to the mean H I velocity, the H I velocities are blueshifted to the south and redshifted to the north and a similar kinematical behaviour is observed for the ^{12}CO velocity field. The ^{12}CO emission appears where two H I components merge into one.

4 DISCUSSION

4.1 Infrared excess regions

In Sections 3.1.1 and 3.2.1, the IR excess was computed using the correlation between DIRBE and Leiden–Dwingeloo data over the whole NCL assuming uniform dust properties and a constant dust to gas ratio. However, dust properties may locally change in cirrus clouds, and the IR excess may simply result from these variations. Four scenarios are therefore possible. First, the IR excess may be entirely the result of changes in the dust properties, of particular dust heating processes or of a peculiar dust-to-gas ratio, without giving information on the molecular gas location. As the Spider and Ursa Major are only exposed to the interstellar radiation field (ISRF), particular dust heating processes do not seem probable. Secondly, the dust properties can locally change across the NCL, but remain uniform within the Spider and Ursa Major fields. In this scenario, the correlation between the 100 μm emission and the H I column density might be different in the Spider and in Ursa

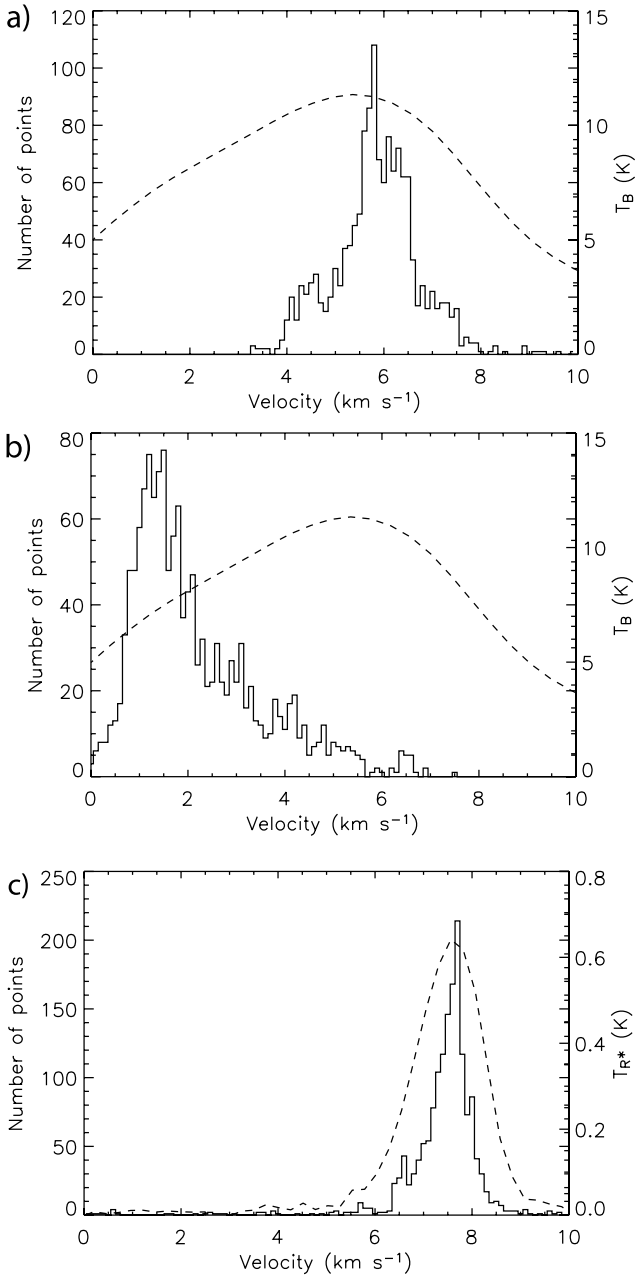

Figure 17. (a) H I NC1 velocity histogram in Ursa Major for the 1394 pixels where ^{12}CO was detected and H I NC1 was observed. The dashed line (right axis) shows the average H I spectrum for these pixels. (b) H I NC2 velocity histogram in Ursa Major for the 1443 pixels where ^{12}CO was detected and H I NC2 was observed. The dashed line (right axis) shows the average H I spectrum for these pixels. (c) ^{12}CO velocity histogram in Ursa Major. The dashed line (right axis) shows the average ^{12}CO spectrum. See Section 3.2.3 for explanations.

Major than for the rest of the NCL. The fields studied in this paper may be different because (i) the dust grains are different (size or shape), (ii) the radiation field is different or (iii) molecule formation affects dust properties. Thirdly, the dust properties can be uniform over the whole NCL, the approach used in Sections 3.1.1 and 3.2.1. Fourthly, if the dust temperature is smaller in the molecular gas, the $N(\mathrm{H})/I_{100\,\mu\mathrm{m}}$ ratios would be larger than the $N(\mathrm{H\,I})/I_{100\,\mu\mathrm{m}}$ ratios computed in this paper. This scenario implies an underestimation of our H_2 column densities.

Table 12. Statistical parameters of the ^{12}CO and H I central velocity distributions in the Ursa Major Cloud.

Component	Mean velocity (km s^{-1})	Standard deviation (km s^{-1})
H I NC1	5.89 ± 0.02	0.88 ± 0.02
H I NC2	2.21 ± 0.04	1.34 ± 0.02
^{12}CO	7.43 ± 0.02	0.90 ± 0.016
Component	Mean line width (σ) (km s^{-1})	Standard deviation (km s^{-1})
H I NC1	1.734 ± 0.009	0.332 ± 0.006
H I NC2	1.56 ± 0.01	0.373 ± 0.007
^{12}CO	0.538 ± 0.004	0.172 ± 0.003

To take into account the possibility of non-uniform dust properties, a joint correlation and a single correlation were locally computed in the Spider and in Ursa Major, respectively, using *IRAS* and DRAO data and new IR excess maps were produced. In these news maps, the extent of the IR excess is similar in the Spider, but five times smaller in Ursa Major. The location of the IR excess peaks does not change. Table 13 provides the physical parameters inferred from the IR excess maps in the Spider and in Ursa Major using the local correlation. The different analysis for the two fields prevents our adopting one of the hypothesis. Future observations from the Planck and Herschel telescopes could address this problem.

As shown in Tables 5, 10 and 13, using the NCL or the local correlation, at least 10 or 18 per cent of the gas is molecular in the Spider while at least 43 or 17 per cent of the gas is molecular in Ursa Major. The ratio between H_2 and H I column densities is also computed using only the pixels with IR excess above 2σ to obtain an upper limit of the fraction of molecular gas. Using the NCL or the local correlation, 33 or 38 per cent of the gas is molecular in the Spider and 50 or 41 per cent of the gas is molecular in Ursa Major. The peak H_2 column densities found in both regions using the IR excess maps are roughly in agreement with the maximal H_2 column densities computed at a higher resolution using the *X* factor on the ^{12}CO data. The mean H_2 column densities are smaller using the IR excess map since smaller H_2 column densities contribute to the mean in the regions where ^{12}CO is not detected. The Spider and Ursa Major have about the same amount of H_2.

In the Spider and in Ursa Major, although there is a strong correlation between the CO and IR excess, the ^{12}CO peaks do not coincide with the IR excess peaks which primarily trace molecular hydrogen. This absence of coincidence between these peaks is often observed. Boulanger et al. (1998) found molecular hydrogen that is not traced by CO in the Chamaeleon molecular clouds. Douglas & Taylor (2007) found that the peak of dust clouds are not spatially coincident with the CO distribution in the Galactic Plane. However, this absence of coincidence between the CO peak and the IR excess peak is not always observed in the literature. In some clouds, the IR excess peak actually coincides with the ^{12}CO peak (Reach et al. 1994). In the Spider and in Ursa Major, the extent of the IR excess ($>2\sigma$) is at least two times larger than the extent of ^{12}CO (above 0.15 K). The absence of CO at some locations where IR excess is observed could have several explanations. Our results do not allow us to choose one, so we will simply discuss four different possibilities.

First, the density could be too low for the excitation of CO ($n(H_2) < 10^3\,cm^{-3}$). In this case, there is CO, but we do not see it. Assuming that the ^{12} CO structures have the same depth as their dimensions on the plane of the sky, we find $n(H_2) \approx 2 \times 10^3\,cm^{-3}$ in the densest region of the Spider and ^{12}CO is readily detected at those densities. However, densities are around $10^2\,cm^{-3}$ at the location of the IR excess peak. At this location, assuming a low density ($n(H_2) = 800\,cm^{-3}$) and the H_2 column density inferred from the IR excess map ($N(H_2) = 4.04 \times 10^{20}\,cm^{-2}$), the depth of the structure should be around 5.6 arcmin. The numbers for size and column density do not present any contradictions. Using the values given in Table 5, an approximation for the shielding factor (Draine & Bertoldi 1996), a canonical value for the H_2 formation rate ($3 \times 10^{-17}\,cm^3\,s^{-1}$; Gry et al. 2002), and assuming a negligible dust opacity for $N(H) < 10^{21}\,cm^{-2}$ (Hollenbach & Tielens 1999), we found that a local balance between H_2 formation and photodissociation occurs at $n(H) \approx 10\,cm^{-3}$. Such a low density confirms that H_2 might be present while CO collisionnal excitation is impossible.

A second possible explanation is insufficient self-shielding. CO may be continually destroyed by the ISRF. This does not exclude the presence of molecules like H_2 at the location of the IR excess since we can detect H_2 without detecting CO (Reach et al. 1998). As the visual extinction (A_V) is smaller in our clouds compared to the translucent clouds, where a coincidence between the IR excess peak and the ^{12}CO was observed (Reach et al. 1994), an insufficient self-shielding is therefore a probable reason for the location discrepancy.

Thirdly, optically thick H I could also cause IR excess, as in Polaris, where Miville-Deschênes (2000) found profiles with features that look like self-absorption. However, according to the least-squares fit, it is impossible to determine if the profile is the result of a cold component in front of a warm component or three components along the line of sight. Inspection of our H I profiles to find self-absorption features is not conclusive. Each possible self-absorption feature that we found can be well explained by two narrow velocity components. Moreover, the maximal column density of our fields is around $6 \times 10^{20}\,cm^{-2}$ compared to $7.6 \times 10^{20}\,cm^{-2}$ for the region in Polaris where self-absorption features were possibly found.

4.2 Molecular observations

In the previous section, the H I–H_2 transition was discussed in the Spider and in Ursa Major using FIR excess as a probe. Some H_2-rich regions were found, but they are not necessarily CO-rich. We will now discuss the transition between the atomic and molecular hydrogen and the CO using H I and CO data. The H I gas is a tracer of the atomic and the molecular hydrogen since H_2 and H I contents are comparable in cirrus clouds for column densities larger than $4 \times 10^{20}\,cm^{-2}$ (Reach et al. 1994). This is in agreement with the fraction of molecular gas found in the regions where the IR excess is larger than 2σ.

The Spider and Ursa Major regions are diffuse high latitude clouds that belong to the same environment, the NCL. Other clouds such as MBM32 (Sakamoto 2002) or the Polaris Flare (Falgarone, Pety & Hily-Blant 2009) also belong to this environment. While a possible rotation towards the Galactic Plane can explain the southern CO blueshifted velocities (with respect to the mean velocity in the Spider and in Ursa Major), the kinematical behaviour of both regions is difficult to reconcile with the large-scale scenario of Pound & Goodman (1997) which involves the expansion of the NCL. According to this scenario, the ^{12}CO velocity should be smaller than the H I velocity, but the ^{12}CO and H I velocities coincide in

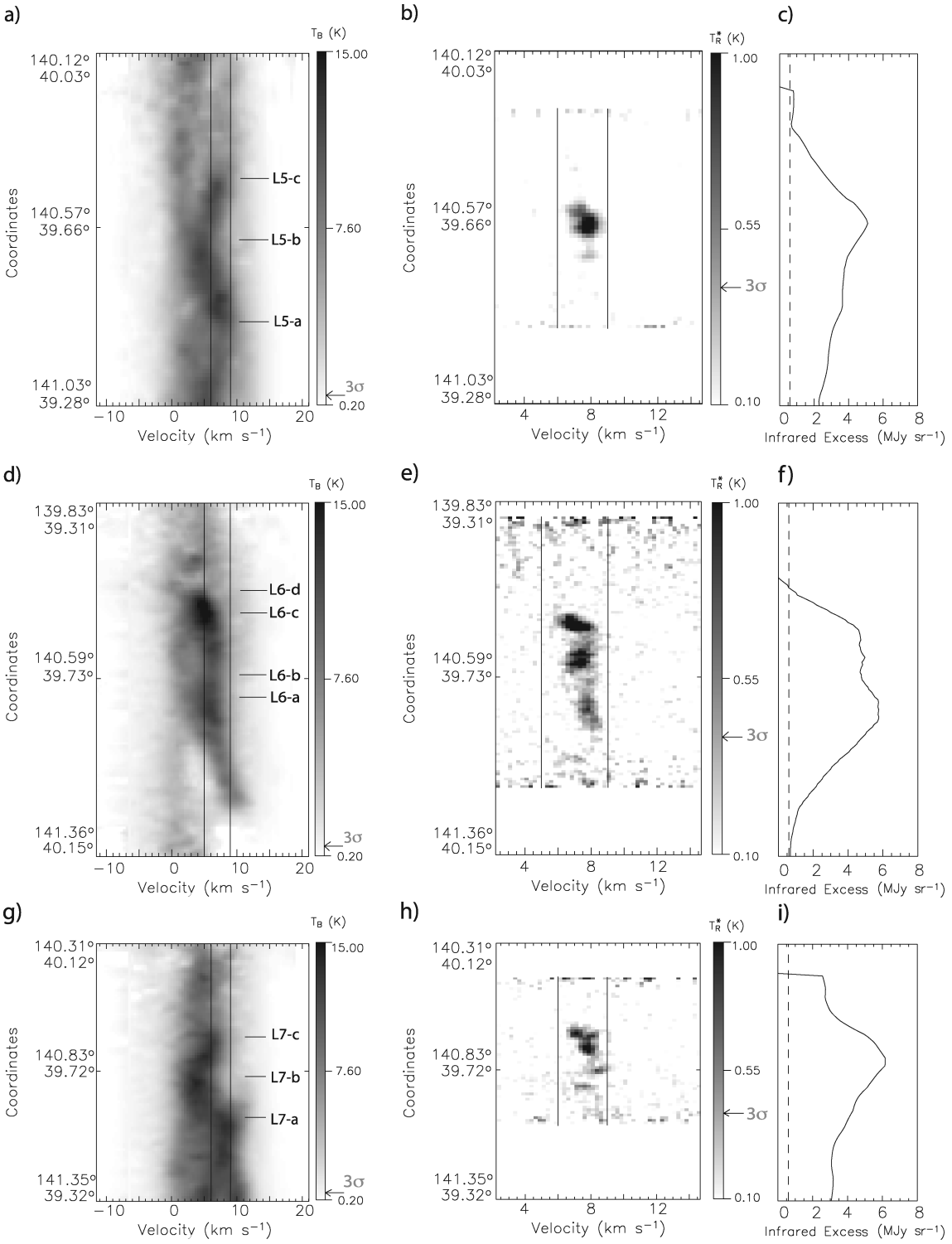

Figure 18. (a) H I position–velocity plot in Ursa Major along line L5 of Fig. 15. (b) ^{12}CO position–velocity plot along the same cut as in (a). (c) IR excess profile along line L5. (d) H I position–velocity plot in Ursa Major along L6 of Fig. 15. (e) ^{12}CO position–velocity plot along the same cut as in (d). (f) IR excess profile along line L6. (g) H I position–velocity plot in Ursa Major along line L7 of Fig. 15. (h) ^{12}CO position–velocity plot along the same cut as in (g). (i) IR excess profile along line L7. Lines are as in Fig. 9.

the Spider, while the velocity difference between both species is almost $+1.7\,\mathrm{km\,s^{-1}}$ in Ursa Major. However, the large-scale scenario cannot be excluded. We are facing two possibilities: a large-scale scenario which relates the H I–H_2 transition to the event which produced the shell and a small-scale one where the H I–H_2 transition is related to the local velocity-shear. These two views complement each other since the event which produced the shell also powered turbulence on small scales.

The coincidence between the ^{12}CO and the H I velocities in the Spider could indicate that molecular and atomic gas are well mixed,

Table 13. Physical parameters inferred from the IR excess distributions using the local correlation.

Parameter	Spider	Ursa
Maximal $N(H_2)$ (10^{20} cm^{-2})	4.11	2.33
All the field		
Mean $N(H_2)$ (10^{20} cm^{-2})	0.48	0.58
Fraction of H_2[1]	0.18	0.17
H_2 Mass ($M_\odot$)	61	10
IR excess ($>2\sigma$)		
Mean $N(H_2)$ (10^{20} cm^{-2})	1.13	1.46
Fraction of H_2[1]	0.38	0.41
H_2 Mass ($M_\odot$)	34	5

[1] $2N(H_2)/(2N(H_2) + N(H\,I))$

keeping in mind that we have only information on the projected velocity along the line of sight. The narrower ^{12}CO line widths could be explained in part by the broader H I thermal line widths. The H I thermal line width is $\approx$0.9 km s^{-1} assuming a temperature of 100 K for the cold H I gas and the ^{12}CO thermal line width is 0.07 km s^{-1} assuming a temperature of 15 K. Subtracting the thermal contribution, the difference between ^{12}CO and H I line widths is $\approx$1.5 km s^{-1}, indicating that the coincidence between both species is incomplete. The mixing between molecular and atomic gas would suggest that molecule formation is currently occurring in the Spider. As shown in the position–velocity cuts, CO seems to appear where two H I velocity components merge into one component or where there is a change in the velocity-shear. The velocity difference between the two H I merging components is larger than 5 km s^{-1}, which is about five times the sound speed in hydrogen at 100 K. ^{12}CO is located in this region where the H I second moment is smaller. This decrease of the H I dispersion can be interpreted as turbulence dissipation (Miville-Deschênes et al. 2002).

In Fig. 9(a), a large velocity-shear ($\approx$44 km s^{-1} pc^{-1}) is seen at the centre of the L1 cut in the area where ^{12}CO emission is strongest. Large velocity-shears ($\approx$29 km s^{-1} pc^{-1}) are also observed at the location of the IR excess peak, but the amount of ^{12}CO is small. The large velocity-shears observed at this location could be interpreted as the signature of a potential site of CO formation in the future. As discussed in the previous section, an H_2 peak is expected in this region.

In the Spider, the H I velocity-shears are not all in the same direction, in agreement with the kinematic behaviour of the H I gas. This absence of a preferential direction and the small extent of H I velocity-shear regions ($\approx$5 arcmin) suggest that CO formation is confined to small areas. Those areas are mostly located in the central regions, to the south along the line L4 of Fig. 6 and to the north at small Galactic longitudes. For the northern and southern CO gas moving with velocities different from the H I velocities, no H I velocity-shear coincides with the CO emission, indicating that molecule formation probably started earlier in those regions. This explains the smaller standard deviation of the H I NC2 velocity histogram compared to the ^{12}CO velocity histogram.

In Ursa Major, contrary to the Spider, the ^{12}CO and H I components are not coincident, but the tails of the velocity histograms overlap in velocity, confirming that both species are related. A different geometry compared to the Spider could explain this velocity difference in Ursa Major. It could also result from the passage of a shock since gas at very different velocities are in contact in a shock. The presence of large velocity gradients in Ursa Major (14 km s^{-1} pc^{-1} to the south of Ursa Major) suggests the presence of shocks (Sakamoto 2002). If the velocity difference between H I and ^{12}CO is attributed to colliding H I features, it explains the larger column densities with respect to the Spider. As in the Spider, CO always appears where two H I components merge, but CO emission is also located between two H I velocity-shears. The H I intensity is smaller at that location. The velocity-shear reaches 50 km s^{-1} in Ursa Major. A small velocity-shear ($\approx$16 km s^{-1}) is observed where IR excess is found, but where ^{12}CO is not detected above the 3σ level (0.3 K). This absence of detection may be caused by the limited sensitivity of the observations, but other molecules could also be formed in those regions. A larger density at the location of the IR excess could increase the H_2 formation rate. No significant velocity-shear is observed where no IR excess is found, confirming the relation between molecule formation and velocity-shear.

The velocity difference observed in Ursa Major compared to the Spider could also be explained if CO formation occurred earlier in Ursa Major compared to the Spider, suggesting that Ursa Major is older than the Spider. This scenario, involving a different evolution stage for those molecular cloud forming sites, is supported by the molecular observations. As shown in Fig. 6, the CO emission is generally twice as strong in Ursa Major as in the Spider for similar H I column densities. Whereas the total molecular mass of the Spider and Ursa Major are similar ($\approx$0.3 $M_\odot$ using the *X* factor method), the mass of the region where ^{13}CO is detected is larger in Ursa Major (0.09 $M_\odot$) than in the Spider (0.03 $M_\odot$).

Since CO does not trace H_2 perfectly, studying in detail the agreement or disagreement between the H I and ^{12}CO line profiles could help to understand the H_2 spatial and velocity distribution. We compare the H I and ^{12}CO line profiles towards the CO peak, the IR peak and the IR excess peak in the Spider and in Ursa Major. Our results show that the velocity difference between CO and H I is bluer at the location of the IR excess peak than at the other locations by $\approx$0.5 km s^{-1} for both fields, but we cannot conclude since the H I velocity resolution is 1.32 km s^{-1} for the Spider and 0.66 km s^{-1} for Ursa Major.

In the Spider and in Ursa Major, we find that CO seems to appear where large H I velocity-shears are observed. Interestingly, Godard, Falgarone & Pineau Des Forêts (2009) predict that CO formation is efficient in H I and H_2 gas where such shears are present. In this model, the dissipation of turbulence allows for molecule formation, even though UV shielding is not as efficient as in giant molecular clouds. Simulations show that H_2 formation can be associated with dynamical behaviours (e.g. Heitsch et al. 2006; Glover & Mac Low 2007; Hennebelle et al. 2008). In turbulent clouds such as the Spider and Ursa Major, the H_2 abundance is expected to be out of equilibrium since the H_2 formation and photodissociation time-scales ($>10^7$ yr) are larger than the dynamical time-scale of the turbulence ($\approx$1 Myr) (Glover & Mac Low 2007). Interestingly, this can explain the absence of correlation between H_2 column density and ^{12}CO emission.

Our results support a scenario in which a transition between atomic and molecular gas occurs. However, another scenario is the inverse transition, in which there is a change of the physical conditions to a less dense and less shielded region such that the molecular state is no longer favoured in steady state. We believe that this scenario does not occur on a large scale since (i) the absence of stars prevents the presence of a strong radiation field that would destroy molecules, (ii) while shocks may destroy molecules since high temperatures are observed behind shocks, the shocks observed

in those cirrus clouds are not strong enough to have a significant effect (Draine & McKee 1993).

5 CONCLUSION

We have discovered two potential sites of H_2 formation in diffuse gas at high Galactic latitude by examining the FIR–H I ratio and looking for an excess over that expected from an atomic medium. We call the first region the Spider and the second region Ursa Major. The IR excess measures could indicate that at least 18 or 10 per cent of the gas is molecular in the Spider while at least 17 or 43 per cent of the gas is molecular in Ursa Major using a local FIR–H I correlation or a correlation over the whole NCL. Between 30 and 50 per cent of the gas is molecular in the regions where the IR excess is above 2σ. ^{12}CO and ^{13}CO ($J = 1 - 0$) emissions were observed in both regions where the IR excess is the highest. The Spider is a fragmented cloud with weak diffuse emission around the high-density regions, and where each region has a different velocity. Ursa Major is also fragmented into many high-density features, but located in an area of strong diffuse emission showing a small velocity gradient. In both regions, the IR excess peaks do not coincide exactly with the ^{12}CO ($J = 1 - 0$) integrated intensity peaks, indicating that CO might be a poor tracer of H_2 in these diffuse regions. While this absence of coincidence can be caused by local variations in the dust properties, it may also be explained by a density too low for the excitation of the ^{12}CO or insufficient self-shielding. As the IR excess could still be coincident with an H_2 peak, the observations of another surrogate molecule, OH, will be useful and will be discussed in a future paper.

The kinematical behaviour of both regions does not support a large-scale scenario involving the NCL, but we cannot reject this scenario since the geometry is unknown. Small-scale motions are probably the main effect that influences the gas kinematics in those regions. CO is observed where two H I velocity components merge into one component or where there is a change in the velocity-shear in agreement with the models that predict that CO formation occurs in the H I and H_2 gas. The velocity difference between CO and H I in Ursa Major could be a signature of colliding H I features where molecules can form. The coincidence between CO and H I velocities in the Spider could indicate that both species are well mixed and that molecule formation probably started earlier in Ursa Major, but the coincidence between both species may be incomplete since the line widths do not agree.

ACKNOWLEDGMENTS

This research was supported by the Natural Sciences and Engineering Research Council of Canada and by the Fonds Québécois de la Recherche sur la Nature et les Technologies. LB acknowledges a doctoral research scholarships from the Fonds Québécois de la Recherche sur la Nature et les Technologies. The DPDF Project was supported by a Special Research Opportunity grant of the Natural Sciences and Engineering Research Council of Canada. The DRAO is operated as a national facility by the National Research Council of Canada. FCRAO was supported by the National Science Foundation (NSF AST-0838222).

REFERENCES

Abergel A., Boulanger F., Delouis J. M., Dudziak G., Steindling S., 1996, A&A, 309, 245
Blitz L., Magnani L., Mundy L., 1984, ApJ, 282, L9
Blitz L., Bazell D., Desert F. X., 1990, ApJ, 352, L13
Boulanger F., Perault M., 1988, ApJ, 330, 964
Boulanger F., Baud B., van Albada G. D., 1985, A&A, 144, L9
Boulanger F., Abergel A., Bernard J., Burton W. B., Desert F., Hartmann D., Lagache G., Puget J., 1996, A&A, 312, 256
Boulanger F., Bronfman L., Dame T. M., Thaddeus P., 1998, A&A, 332, 273
Cecchi-Pestellini C., Casu S., Dalgarno A., 2005, MNRAS, 364, 1309
Chang Q., Cuppen H. M., Herbst E., 2005, A&A, 434, 599
Charbonneau P., 1995, ApJS, 101, 309
de Vries H. W., Thaddeus P., Heithausen A., 1987, ApJ, 319, 723
Désert F. X., Bazell D., Boulanger F., 1988, ApJ, 334, 815
Désert F.-X., Boulanger F., Puget J. L., 1990, A&A, 237, 215
Dickman R. L., 1978, ApJS, 37, 407
Douglas K. A., Taylor A. R., 2007, ApJ, 659, 426
Draine B. T., Bertoldi F., 1996, ApJ, 468, 269
Draine B. T., McKee C. F., 1993, ARA&A, 31, 373
Dutra C. M., Bica E., 2002, A&A, 383, 631
Falgarone E., Phillips T. G., 1996, ApJ, 472, 191
Falgarone E., Puget J.-L., 1995, A&A, 293, 840
Falgarone E., Pineau des Forets G., Roueff E., 1995, A&A, 300, 870
Falgarone E., Pety J., Hily-Blant P., 2009, A&A, 507, 355
Federman S. R., Glassgold A. E., Kwan J., 1979, ApJ, 227, 466
Feigelson E. D., Babu G. J., 1992, ApJ, 397, 55
Flower D. R., Pineau des Forets G., 1998, MNRAS, 297, 1182
Gillmon K., Shull J. M., 2006, ApJ, 636, 908
Gillmon K., Shull J. M., Tumlinson J., Danforth C., 2006, ApJ, 636, 891
Glover S. C. O., Mac Low M., 2007, ApJ, 659, 1317
Godard B., Falgarone E., Pineau Des Forêts G., 2009, A&A, 495, 847
Gry C., Boulanger F., Nehmé C., Pineau des Forêts G., Habart E., Falgarone E., 2002, A&A, 391, 675
Hartmann D., Burton W. B., 1997, Atlas of Galactic Neutral Hydrogen. Cambridge Univ. Press, Cambridge
Hartmann D., Magnani L., Thaddeus P., 1998, ApJ, 492, 205
Haud U., 2000, A&A, 364, 83
Hauser M. G. et al., 1998, ApJ, 508, 25
Heiles C., 1975, A&AS, 20, 37
Heiles C., Habing H. J., 1974, A&AS, 14, 1
Heiles C., Troland T. H., 2003, ApJ, 586, 1067
Heithausen A., 1996, A&A, 314, 251
Heithausen A., Bertoldi F., Bensch F., 2002, A&A, 383, 591
Heitsch F., Slyz A. D., Devriendt J. E. G., Hartmann L. W., Burkert A., 2006, ApJ, 648, 1052
Hennebelle P., Banerjee R., Vázquez-Semadeni E., Klessen R. S., Audit E., 2008, A&A, 486, L43
Hennebelle P., Mac Low M.-M., Vazquez-Semadeni E., 2009, in Chabrier G., ed., Structure Formation in Astrophysics. Cambridge Univ. Press, Cambridge, p. 205
Heyer M., Krawczyk C., Duval J., Jackson J. M., 2009, ApJ, 699, 1092
Hollenbach D. J., Tielens A. G. G. M., 1999, Rev. Mod. Phys., 71, 173
Ingalls J. G., Bania T. M., Lane A. P., Rumitz M., Stark A. A., 2000, ApJ, 535, 211
Isobe T., Feigelson E. D., Akritas M. G., Babu G. J., 1990, ApJ, 364, 104
Joncas G., Boulanger F., Dewdney P. E., 1992, ApJ, 397, 165
Lagache G., Haffner L. M., Reynolds R. J., Tufte S. L., 2000, A&A, 354, 247
Landecker T. L. et al., 2000, A&AS, 145, 509
Liszt H. S., 2007, A&A, 476, 291
Liszt H., Lucas R., Pety J., 2005, in Lis D. C., Blake G. A., Herbst E., eds, Proc. IAU Symp. 231, Astrochemistry Throughout the Universe: Recent Successes and Current Challenges. Cambridge Univ. Press, Cambridge, p. 187
Low F. J. et al., 1984, ApJ, 278, L19
McGehee P. M., 2008, in Reipurth B., ed., Handbook of Star Forming Regions, Volume II: The Southern Sky. Astron. Soc. Pac., San Francisco, p. 813
Magnani L., Hartmann D., Speck B. G., 1996, ApJS, 106, 447

Markwardt C. B., 2009, in Bohlender D. A., Durand D., Dowler P., eds, ASP Conf. Ser. Vol. 411, Astronomical Data Analysis Software and Systems XVIII. Astron. Soc. Pac., San Francisco, p. 251
Martin R. N., Barrett A. H., 1978, ApJS, 36, 1
Meyerdierks H., Heithausen A., Reif K., 1991, A&A, 245, 247
Miville-Deschênes M.-A., 2000, PhD thesis, Univ. Laval
Miville-Deschênes M.-A., Lagache G., 2005, ApJS, 157, 302
Miville-Deschênes M.-A., Boulanger F., Joncas G., Falgarone E., 2002, A&A, 381, 209
Miville-Deschênes M., Joncas G., Falgarone E., Boulanger F., 2003, A&A, 411, 109
Nehmé C., Le Bourlot J., Boulanger F., Pineau Des Forêts G., Gry C., 2008, A&A, 483, 485
Pound M. W., Goodman A. A., 1997, ApJ, 482, 334
Reach W. T., Koo B.-C., Heiles C., 1994, ApJ, 429, 672
Reach W. T., Wall W. F., Odegard N., 1998, ApJ, 507, 507
Rohlfs K., Wilson T. L., 2000, Tools of Radio Astronomy. Springer, Berlin
Sakamoto S., 2002, ApJ, 565, 1050
Spaans M., 1996, A&A, 307, 271
Starck J., Murtagh F., 1998, PASP, 110, 193
Stark R., Dickey J. M., Burton W. B., Wennmacher A., 1994, A&A, 281, 199
Taylor A. R. et al., 2003, AJ, 125, 3145
Turner B. E., Terzieva R., Herbst E., 1999, ApJ, 518, 699
van Dishoeck E. F., Black J. H., 1986, ApJS, 62, 109
van Dishoeck E. F., Black J. H., 1988, ApJ, 334, 771
van Dishoeck E. F., Black J. H., Phillips T. G., Gredel R., 1991, ApJ, 366, 141
Wakker B. P., 2006, ApJS, 163, 282
Weiland J. L., Blitz L., Dwek E., Hauser M. G., Magnani L., Rickard L. J., 1986, ApJ, 306, L101
Yamamoto H., Onishi T., Mizuno A., Fukui Y., 2003, ApJ, 592, 217

This paper has been typeset from a TEX/LATEX file prepared by the author.